

Modified Fluid Closure of Weakly-Collisional Plasmas in Radiatively-Inefficient Accretion Flows

Lia Hankla

Advisor: James Stone. Co-advisor: Frans Pretorius

May 1, 2017

Abstract

The diversity of plasmas in nature divides their study into many different regimes which are valid only within certain approximations. This paper attempts to extend the validity of one such regime (a fluids framework) to another (kinetic theory, for collisionless plasmas). The focus is more narrowly on astrophysical systems, where studies of collisionless plasmas very often use the fluid model which should theoretically not apply. Recent kinetic simulations of black hole accretion flows make radiatively inefficient accretion flows an ideal starting point to investigate the possibility of using a modified fluids closure to model collisionless plasmas. If the fluid regime is found to be an appropriate model, then the door is opened for future work on global simulations and other weakly collisional plasmas. Study of these accretion flows is done through three-dimensional local shearing box magnetohydrodynamic simulations with anisotropic viscosity and a maximum pressure anisotropy, a choice motivated by the aforementioned kinetic simulations.

Contents

1	Introduction	3
1.1	Overview	3
1.2	Collisionless and Weakly Collisional Plasmas	4
1.3	Motivation and Impacts	6
2	Background	8
2.1	Plasma Physics	8
2.1.1	Characteristic Plasma Parameters	9
2.1.2	Vlasov Kinetic Theory	10
2.1.3	Single-fluid MHD	11
2.1.4	Braginskii MHD	14
2.1.5	Kinetic effects closure	17
2.2	Codes: Athena4.2 and Pegasus	17
2.3	Early Problems in Accretion	18
3	Computational Context Through the MRI	21
3.1	Local Ideal MHD Theory and Simulations	21
3.1.1	Ideal MRI Condition for Stability and Maximum Growth Rate	23
3.1.2	Spring Interpretation	27
3.1.3	Shearing Box Method	28
3.2	Local Non-ideal MHD Theory and Simulations	29
4	Modified Fluid Closure of a Collisionless Plasma	33
4.1	Progress	33
	Bibliography	42

Chapter 1

Introduction

1.1 Overview

The discipline of plasma physics encompasses a vast variety of plasmas, stretching from earthly laboratory-made fusion plasmas to astrophysical plasmas such as the intracluster medium and accretion flows onto compact objects. What separates this discipline into different subfields is the immense variety of scales in terms of distance, density, and temperature. Although the theory of magnetohydrodynamics is scale-less, the different relationship between parameters means that the plasma inside a tokamak is not usefully described by the same set of equations as a disk of matter around the black hole at the center of the galaxy, where the distances are tens of orders of magnitude greater, densities are tens of orders of magnitude times smaller, and temperatures ten times lower (see Table 1.1).

All plasmas can in principle be described by a collection of equations describing the Lorentz force and other interactions on every single particle in the plasma. As can easily be imagined, however, the task of following billions of particles is intractable both analytically and computationally. Different sets of assumptions allow the impossible equations to be reduced to something useful in their respective situations. For instance, plasmas in which the particles do not collide often if at all (termed “weakly collisional” or “collisionless”, respectively), need to be evolved using a distribution function that takes into account the spread of particle velocities: a kinetic theory. In contrast, when the particles in a plasma collide many many times before they travel any meaningful distance in a system, the plasma can be treated as a fluid. Said fluid has only one, “bulk”, velocity at any given point. The

fluid mechanical approach is a further simplification of the full kinetic theory. As such, we would not expect a fluid treatment of weakly collisional plasmas to hold much weight.

It is perhaps surprising then, that it is common practice to do so. This unjustified assumption is not so hard to understand given the conceptual and practical simplification that the fluids model presents: instead of evolving six degrees of freedom, there are only three. It is more intuitive to think about fluids as we have every day experience with them. Another reason is simply the inability to make progress otherwise: as late as 2011 kinetic simulations were still “well beyond our present capability” [1]. So is this assumption valid? To date an investigation of the validity of this assumption seems to be absent from the astrophysical literature, although similar works may exist in the fusion literature without my knowledge.

The main goal of this thesis is to explore the viability of modelling a weakly collisional plasma with a modified fluid closure. If such an approximation is found to exist, then the assumptions of the past studies listed above are validated and the works stand on firmer theoretical ground. The approximation would also path the way for further studies of weakly collisional and collisionless plasmas, easing not only the conceptual difficulty of a full kinetic theory but also the computational nuisance of particle-in-cell (PIC) simulations, which are limited by the extreme amount of resources they consume (a PIC simulation that takes millions of cpu-hours can be done in tens of cpu-hours using a fluid model).

1.2 Collisionless and Weakly Collisional Plasmas

More formally, a collisionless plasma is one for which the particles on average travel longer than the scales one is interested in without colliding. This means that the length scale of interest (the radius of an accretion disk, for example, or the distance between the sun and the earth for the solar wind) L is much less than the mean free path λ_{mfp} of particles. In these cases the magnetic field is also strong enough such that the Larmor radius ρ is much less than both length scales of interest and the mean free path (a so-called “magnetized” plasma). We therefore have the ordering

$$\rho \ll L \ll \lambda_{mfp} \tag{1.1}$$

For weakly collisional plasmas, the mean free path is on the order of the length scales of interest: $\rho \ll L \sim \lambda_{mfp}$. These orderings are opposed to fluid models in which both the mean free path and the Larmor radius are much less than the length scales of interest ($\lambda_{mfp} \ll L, \rho \ll L$). The range of systems underneath the “collisionless” and “weakly collisional” plasma umbrella is still quite large and therefore worth studying. Collisionless plasmas are most typically found in the solar wind [2–4], while canonical weakly collisional plasmas are the intracluster medium between galaxies [5–7] and radiatively inefficient accretion flows (RIAFs) around black holes. Table 1.1 shows these collisionless and weakly collisional plasmas’ parameters in comparison to collisional plasmas such as magnetically-confined fusion plasmas [8].

Radiatively-inefficient accretion flows (RIAFs) are often treated as a fluid, usually with qualifications about such ad hoc assumptions [9–16]. RIAFs are mainly found in two situations: binary systems and active galactic nuclei. Figure 1.1 shows illustrations of these two main regimes. Binary systems involve black holes on the order of tens of solar masses. In this regime it is hoped that the RIAF model can explain observations of x-ray binary outbursts, or transitions from the dormant quiescent soft state to the active hard state and vice versa [17–21] (other possible explanations include the very complex phenomenon of black hole jets [22–24]; see [25] for a review). This thesis will concentrate on the other regime of RIAFs around supermassive black holes like Sagittarius A*, the one at the center of the galaxy.

Although other black holes like M87 [26–29] and GX 339-4 [30] have been studied, much of the literature focuses on Sagittarius A* due to its proximity. The accretion disk around this black hole is many times dimmer than one might expect, knowing that the gravitational energy of in-falling matter must go somewhere—and where does it go, if not into radiation that can then be detected on Earth? Current models suggest that the accretion disk is heated up, resulting in a hot flow whose mean free path between particles is correspondingly large: a weakly collisional plasma. Such flows are termed “radiatively inefficient accretion flows” (RIAFs) and are thought to effectively model low-luminosity active galactic nuclei (LLAGN) such as Sagittarius A* [1, 9, 31–33]. With the Event Horizon Telescope [34], models that accurately explain observations are becoming even more crucial.

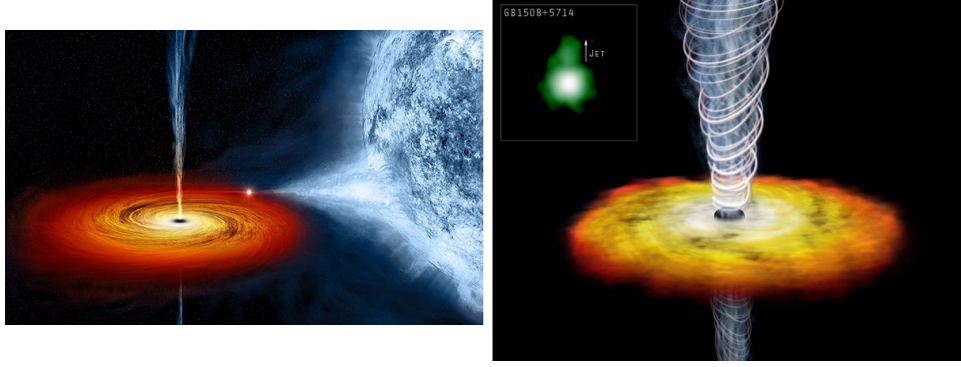


Figure 1.1: Artists’ renderings of accretion disks. Left: accretion from a white dwarf onto a black hole. The accretion disk is in orange. Relativistic jets are shown launching out of the disk. Image from Siemiginowska and Weiss [35]. Right: around a supermassive black hole, supported by an image taken by the Chandra X-ray Observatory (inset). The disk itself is in orange, while magnetic field lines are shown in white around the collimated jets. Image from Luminet [36].

1.3 Motivation and Impacts

This thesis will concentrate on weakly collisional plasmas in the context of RIAFs. This choice is motivated both by a recent paper that presents the first kinetic simulation of how accretion in a RIAF happens locally [38] and by hints at the inability of a fluid model to capture the correct growth rates of kinetic phenomena [39]. Although there has been some study on modified fluid closures to capture kinetic physics [40–43], these studies use a different formalism and could only be compared to 2D simulations. Now that a 3D kinetic simulation has been performed by Kunz et al. [38], a direct comparison between a modified fluid closure and kinetic theory is possible. The paper uses methods that are easily replicated using the Athena code developed by Stone et al. [44], in particular the same local shearing-box method [45]. A comparison is thus easily facilitated and meaningful.

This paper is complementary to other current research in the field of accretion disk physics that often assumes a high degree of collisionality. For example, there is a push to include general relativity in accretion disk calculations in order to describe observations [20, 21, 26, 46–53]. This paper addresses the fundamental assumptions of these papers and assesses their

	L (cm)	n (cm ⁻³)	T (eV)	B (G)	ρ (cm)	λ_{mfp} (cm)
ICM	6.2e23	5.0e-3	8.0e3	1.0e-6	1.3e10	9.5e21
RIAFs	3e17	1.0e2	2.0e3	1.0e-3	1e6	1e16
Solar wind	1.5e13	1.0e1	1.0e1	1.0e-4	4.6e6	1.2e13
ISM	3.1e20	1.0e0	1.0e0	5.0e-6	2.9e7	1.3e12
JET	1.0e2	1.0e14	1.0e4	3.0e4	4.8e-1	1.4e6

Table 1.1: Comparison of parameters of different plasmas found in space and on earth. ICM: intracluster medium. ISM: interstellar medium. JET: Joint European Torus (a tokamak). Collisionless and weakly collisional plasmas are above the horizontal lines; collisional plasmas are below. Numbers calculated from parameters given in [8, 37].

validity, providing the groundwork for extending magnetohydrodynamics to relativistic systems and other effects.

A fluid closure to kinetic physics has consequences beyond just black hole accretion. If proper parameters are found that sufficiently imitate the kinetic physics of RIAFs, then this model can be extended to global simulations and enables the exploration of the parameter space of other collisionless and weakly collisional plasmas. Such exploration is currently prohibitively expensive computationally as mentioned previously because PIC simulations are required. If a fluid model is achieved, then the simulations are much more manageable, allowing for more thorough scans of, for example, magnetic field strength. A fluid model closure to kinetic physics is also interesting in a conceptual sense since it would mean that the six phase-space degrees of freedom could be reduced to only three position-space degrees of freedom.

The structure of this paper is as follows: the necessary background to understand the fundamental plasma physics question is explained in Chapter 2.1. The actual physical mechanism for accretion, a linear MHD instability called the magnetorotational instability (MRI), is outlined in Chapter 3 using both analytic theory and the main tool of the rest of this thesis—simulations. Building from the simplest MHD theory (ideal MHD) to more complex, resistive MHD, we transition into the original research of this thesis, found in Chapter 4. Chapter 4 uses anisotropic viscosity along magnetic field lines in an attempt to capture kinetic physics with a modified fluid closure.

Chapter 2

Background

The ultimate goal of this thesis is to study a particular phenomenon (the MagnetoRotational Instability, MRI) in a particular regime (anisotropic viscosity) of plasma physics. In order to do so, it is helpful to be acquainted with the various plasma physics formalisms. This will be accomplished in Section 2.1. The numerical codes in use are explained in Section 2.2, while the reason accretion is not trivial is outlined historically in Section 2.3.

2.1 Plasma Physics

Plasma physics applies to a wide range of subject areas, from magnetic-confinement fusion pursuits like the tokamak ITER [54] and the stellarator Wendelstein 7-X [55] to a variety of astrophysical situations, including the sun’s corona and protoplanetary disks. The uniting theme across these different disciplines is the plasma: so what exactly is a plasma?

A plasma is the so-called “fourth state of matter”, coming after the gas phase in the increasing kinetic energy hierarchy solid-liquid-gas: that is, the kinetic energy of a plasma particle is much greater than its potential energy. A plasma is made up of neutrals and the result of the neutrals’ ionization: that is, ions and electrons. The basic physics of single-particle motion in electric and magnetic fields (for example, ∇B drift and $E \times B$ drift) apply to every single particle. Given the enormous quantity of particles, working analytically or simulating such a situation for each individual particle is near impossible. Indeed, this is why the kinetic theory is so complicated and requires particle-in-cell simulations that use codes such as PEGASUS (Section 2.2). The task of this thesis is to make simulations feasible via

(modified) fluid equations.

2.1.1 Characteristic Plasma Parameters

One parameter that will be frequently discussed (since it determines the model that describes a plasma) is the mean free path λ_{mfp} of a plasma particle, that is, how far it travels on average before it collides with another particle. This is related to the thermal velocity $v_T = \sqrt{2T/m}$ and collision frequency ν by

$$\lambda_{mfp} = \frac{v_T}{\nu} = \frac{1}{\nu} \sqrt{\frac{2T}{m}} \quad (2.1)$$

Notice that since the mass of an electron is so small compared to that of an ion (made up of protons and neutrons), the electron thermal velocity is much greater than the ion thermal velocity.

The collision frequency ν depends on the temperature and density of a species as

$$\nu \sim nT^{-3/2} \quad (2.2)$$

Hence an increase in temperature leads to an increase in the mean free path of a particle because it decreases the collision frequency. In general, a higher collision rate simplifies calculations [56]. This is because collisions push particles towards the Maxwell-Boltzmann (or Maxwellian) distribution of thermal equilibrium. Ideal MHD assumes a Maxwellian distribution. It is departures from this equilibrium that complicate calculations.

Now we turn to defining magnetization in plasmas, which is an important definition in Braginskii MHD. The most important parameter is the easily-derivable thermal gyroradius: $\rho_s \equiv v_{Ts}/\Omega_s$ where $\Omega_s = q_s B/m_s$ (Gaussian units). A magnetized plasma is one for which the dimensionless parameter $\delta \equiv \rho/L$ goes to zero. In this case, particles will follow orbits that oscillate many times about magnetic field lines as their guiding center travels along the field lines. In ideal MHD, both $\lambda_{mfp} \ll L$ and $\delta \ll L$, whereas Braginskii MHD takes $\rho \ll \lambda_{mfp} \ll L$ and a collisionless plasma has $\lambda_{mfp} \gtrsim L$.

As will be explained more later, the balance of magnetic pressure to gas pressure is also an important parameter. The plasma parameter, or β , as it is called, is given by:

$$\beta = \frac{8\pi P}{B^2} \quad (2.3)$$

where P is the plasma pressure and B is the magnetic field. β is generally much larger in astrophysical systems (order of hundreds or thousands) than in magnetic-confinement fusion, where β is usually around .01.

Having established some basic properties of a plasma, we can now investigate some theories to model them, starting with kinetic theory.

2.1.2 Vlasov Kinetic Theory

Kinetic theory generalizes the brute-force method of applying Maxwell's equations (and the Lorentz Force Law) to many particles. The main result, known as the Vlasov equation, is:

$$\frac{\partial f_s(\vec{x}, \vec{v}, t)}{\partial t} + \vec{v}_k \frac{\partial f_s}{\partial x_k} + \frac{q}{m} (\vec{E} + \frac{\vec{v}}{c} \times \vec{B})_k \frac{\partial f_s}{\partial v_k} = C[f_s] \quad (2.4)$$

where f_s is the phase-space density, or distribution function, and \vec{v} is the velocity of a particle with charge q and mass m in electric and magnetic fields \vec{E} and \vec{B} . The left side depends only smoothly-varying terms, whereas the right is spiky, being the average of products of delta functions. The right-hand side represents the interactions between individual particles, and we can lump all these effects into the so-called "collision operator" $C[f]$. Entire graduate courses can be taught on the collision operator so we will not delve too much into it here.

We define the distribution function to be normalized such that:

$$\rho(\vec{x}, t) = \int d^3\vec{v} f(\vec{x}, \vec{v}, t) \quad (2.5)$$

where ρ is the mass density and we have summed over species. Conservation laws emerge by taking different moments of the Vlasov equation and the collision operator. The k -th moment is defined as taking the integral $\int d^3v v^k f_s$. Such moments are usually done in the frame moving with the bulk velocity of the fluid such that $\vec{v} \rightarrow \vec{v} - \vec{u}$ here. Particle conservation, for example, arises from taking the zeroth-moment of the distribution function.

A problem arises, however: every conservation law involves a higher moment of the distribution function. The evolution of density involves velocity, evolution of velocity involves the pressure tensor \vec{P} , evolution of the pressure involves the heat flux tensor \vec{Q} , and so on. This pattern of always involving higher moments of the distribution function does not simply disappear.

Rather, it is a central problem of plasma physics known as the BBGKY hierarchy. It is various choices to “close” this loop of higher moments that defines different theories, including the standard ideal or “single-fluid” MHD.

Methods to close the moment equations fall broadly into three categories: truncation, cases with special values for the distribution function or stress tensor, and asymptotic methods. The most straightforward solution is to simply truncate the hierarchy: just call the heat flux tensor $\vec{Q} = 0$. This method can lead to useful intuition, but also means that the amount of error is not well-accounted for at all. There are also special cases such as having a Maxwellian distribution function (and thus assuming local thermal equilibrium) or assuming a cold plasma that eliminate the need for the fourth moment equation [56]. The last closure method is that of asymptotics. This method generally assumes an ordering of certain parameters and expands about small values; which parameters are large or small depends on the exact type of asymptotic closure. This method is thereby more rigorous and the one that leads to ideal and Braginskii MHD, discussed below.

The standard so-called “MHD ordering” assumes a magnetized plasma and takes $\delta \equiv \rho/L \ll 1$. Assumptions from this point forward divide MHD into its different branches (for example, single-fluid ideal MHD and Braginskii MHD) and will be discussed in subsequent sections.

2.1.3 Single-fluid MHD

In single-fluid MHD, all species are treated as a single fluid. That is, to lowest-order they all have the same temperature and flow velocity and we average out the individual particles’ positions and velocities. The important quantities are bulk variables, like the mean flow of the fluid, density, and pressure (one can already see how these variables might not make as much sense for an extremely diffuse plasma such as the weakly collisional ones described in Chapter 1).

We consider MHD with the transport coefficients η and ν , the resistivity and shear viscosity, respectively. Ideal MHD can be obtained by setting these numbers to zero. The full set of equations is the moment equations

combined with Maxwell's equations:

$$\frac{\partial \rho}{\partial t} + \nabla \cdot (\rho \vec{v}) = 0 \quad (2.6)$$

$$\rho \frac{\partial \vec{v}}{\partial t} + (\rho \vec{v} \cdot \nabla) \vec{v} = -\nabla P + \frac{1}{4\pi} (\nabla \times \vec{B}) \times \vec{B} + \nu \left(\nabla^2 \vec{v} + \frac{1}{3} \nabla (\nabla \cdot \vec{v}) \right) \quad (2.7)$$

$$\frac{Dp}{Dt} + \frac{5}{3} p \nabla \cdot \vec{v} = 0 \quad (2.8)$$

$$\frac{\partial \vec{B}}{\partial t} = \nabla \times (\vec{v} \times \vec{B} - \eta \nabla \times \vec{B}) \quad (2.9)$$

Here, the “convective derivative” $\frac{D}{Dt} = \frac{\partial}{\partial t} + \vec{v} \cdot \nabla$, where \vec{v} is the center of mass motion of the fluid. This derivative accounts for both temporal and spatial variation as a fluid element moves along with the bulk motion of the rest of the fluid. The adiabatic index γ depends on the equation of state. Isothermal evolution ($P = \rho c^2$, where c is the speed of sound) takes $\gamma = 1$. This thesis will consider adiabatic evolution with $\gamma = 5/3$, that of a monatomic ideal gas.

The moment equations are the first two equations, known respectively as the continuity and momentum equation, with Maxwell's equations slipped into the momentum equation and appearing as the induction equation (2.9). This can be seen by considering Ohm's law: $\vec{J} = \sigma(\vec{E} + \frac{1}{c} \vec{v} \times \vec{B})$, where σ is the plasma conductivity. Combining with Ampere's law $\vec{J} = \frac{c}{4\pi} \nabla \times \vec{B}$ after neglecting the displacement currents since the fluid is nonrelativistic, we have $\vec{E} = \frac{c}{4\pi\sigma} \nabla \times \vec{B} - \frac{1}{c} \vec{v} \times \vec{B}$. Now using Faraday's law, we have $\frac{1}{\sigma} \nabla \times \vec{J} - \frac{1}{c} \nabla \times (\vec{v} \times \vec{B}) = -\frac{1}{c} \frac{\partial \vec{B}}{\partial t}$, which leads to the induction equation after identifying $\eta = c^2/4\pi\sigma$. The other Maxwell's laws are contained in the assumption of quasi-neutrality $\sum_s n_s q_s = 0$ (Gauss's law) and by imposing the initial condition $\nabla \cdot \vec{B} = 0$, which will then remain true.

We can use a vector identity to make the separation of the magnetic field energy into two components obvious: $(\nabla \times \vec{B}) \times \vec{B} = (\vec{B} \cdot \nabla) \vec{B} - (\nabla \vec{B}) \cdot \vec{B} = (\vec{B} \cdot \nabla) \vec{B} - \frac{1}{2} \nabla B^2$ where $B^2 = \vec{B} \cdot \vec{B}$. The magnetic pressure ∇B^2 term tries to increase the spacing between magnetic field lines, making the parallel with normal pressure more obvious. The magnetic tension term $-\vec{B} \cdot \nabla \vec{B}$ term tries to unfurl curves in magnetic field lines. This term plays an important role in the mechanism of accretion discussed in Chapter 3.1.2.

In ideal MHD, the magnetic field lines cannot diffuse since the plasma is

perfectly conducting. This means that the field lines are effectively frozen into the plasma: the phenomenon is appropriately called “flux-freezing”, or alternatively as Alfvén’s Theorem. Flux-freezing has important consequences for turbulence, since if a fluid particle is perturbed slightly, it will drag the magnetic field line with it. In non-ideal MHD, the field lines slip with respect to the rest of the plasma on the time scale of $\tau_R = \frac{\mu_0 L^2}{\eta}$. This time scale will become important in Chapter 3: for instance, if the dissipation time scale is shorter than characteristic time scales of the system (such as orbital time), then the magnetic field will decrease in energy, hindering the development of a magnetic dynamo.

Non-ideal MHD carries with it a number of dimensionless numbers that characterize the relative importance of various quantities. For example, the Reynolds number is given by the ratio of inertial forces to viscous forces and can be written as $\text{Re} = \frac{c_0 H^2}{H \nu} = \frac{c_0 H}{\nu}$ where c_0 is the sound speed or other characteristic velocity in the fluid and ν is the viscosity. H is the characteristic length scale, which here we take as the scale height of the disk. Thus the Reynolds number is the amount of dissipation on disk length scales in one sound crossing.

The magnetic Reynolds number describes how important induction and advection of the magnetic field is compared to momentum advection of a fluid, while the ratio of the magnetic Reynolds number to the Reynolds number is called the magnetic Prandtl number:

$$\text{Pm} = \frac{\text{Re}_M}{\text{Re}} = \frac{\nu}{\eta} \quad (2.10)$$

The magnetic Prandtl number accordingly measures how important viscous diffusion is relative to resistive diffusion. Higher Prandtl number means viscous dissipation is more important, and thus the velocity field is smoothed more than the magnetic field. In such situations we can expect more small-scale magnetic field eddies than velocity eddies. The hydrodynamic Prandtl number measures the importance of viscosity as compared to thermal diffusion and heat conduction rather than resistivity [57].

The importance of resistivity and viscosity has been explored in a number of papers [57–59] and plays an important role in the physics of accretion, as will be discussed in Chapter 3.

Since the point of this thesis is that MHD is not valid for certain kinds

of plasmas, let us now examine the assumptions that went into these equations. We first assume that pressure is isotropic, which means the heat flux tensor disappears. Since we are here considering magnetized plasmas, we also take $\delta = \rho/L \rightarrow 0$. Quasi-neutrality is a good simplification since plasmas are usually overall neutral in nature. Dropping the displacement current in Ampere's law is also fine, since as mentioned earlier, the characteristic velocity of particles in our system is the thermal velocity. Note that it is possible to include general relativity in these calculations; however, as mentioned in the introduction, this thesis is concerned with the limit in which general relativity is excessive.

Lifting the requirement that pressure be isotropic and introducing a new ordering of scales leads to Braginskii MHD, described in the following section.

2.1.4 Braginskii MHD

Braginskii MHD uses the assumptions that the time between collisions, while not zero, is much larger than typical time scales. Equivalently, the collisional frequency is much greater than other characteristic frequencies of the system. The appropriate limits are:

$$\rho \ll \lambda_{mfp} \ll L \quad (2.11)$$

Note that weakly collisional systems have mean free paths comparable to or larger than the length scales of the system: we therefore have no apparent reason to trust Braginskii MHD in a weakly collisional regime! Such is the motivation of this thesis: we shall investigate whether we can actually accomplish a meaningful approximation.

Because the magnetic field is so strong and the gyromagnetic radius is so small compared to the mean free path, we can write the motion of particles as a sum of the guiding center motion and the gyrotropic motions about the field lines. This leads to an anisotropic pressure tensor

$$\begin{pmatrix} p_{\parallel} & 0 & 0 \\ 0 & p_{\perp} & 0 \\ 0 & 0 & p_{\perp} \end{pmatrix} \quad (2.12)$$

if $\hat{x} = \hat{b}$ is along the magnetic field. Note that the isotropic pressure $p = \frac{2}{3}p_{\perp} + \frac{1}{3}p_{\parallel}$ and hence $p_{\perp} = p + \frac{1}{3}(p_{\perp} - p_{\parallel})$ and $p_{\parallel} = p - \frac{2}{3}(p_{\perp} - p_{\parallel})$.

Rigorously what follows is an expansion of the distribution function about a Maxwellian (see, e.g., [60]). However, we take a more intuitive approach here and simply argue for adding collisional terms to the evolution equations for the pressures, which arise from conservation of adiabatic invariants.

Adiabatic Invariants are quantities that are “conserved” in the sense that they stay the same when changes in a system happen slowly enough. The two that we consider here are the magnetic moment μ and the mirror constant J :

$$\mu = \frac{1}{2}m \frac{w_{\perp}^2}{B} \qquad J \equiv m \oint w_{\parallel} dl$$

These are conserved as long as $|\frac{D \ln B}{Dt}| \ll \Omega$ and $|\frac{D \ln B}{Dt}| \ll \omega_b$ where ω_b is the bounce frequency associated with the magnetic mirror under consideration. Following Kunz [61], we see how these invariants relate the anisotropic pressure and the magnetic field:

$$\langle \mu \rangle \sim \frac{p_{\perp}}{Bn} = \frac{T_{\perp}}{B} \qquad \langle J^2 \rangle \sim \frac{mB^2}{n^3} p_{\parallel} = \frac{B^2}{n^2} T_{\parallel} m \quad (2.13)$$

with $T_{\parallel, \perp} = p_{\parallel, \perp}/n$. An increase in the magnetic field strength will lead to an increase in perpendicular pressure, which will increase the pressure anisotropy. Combining these equations, we can come up with an equation for the evolution of the pressure anisotropy. We know that collisions push the distribution function back to a Maxwellian; therefore, we keep the pressure anisotropy small, moderated by the small parameter ν_{coll} :

$$\begin{aligned} \frac{Dp_{\perp}}{Dt} &= p_{\perp} \left(\frac{D \ln Bn}{Dt} \right) - \nu_{coll}(p_{\perp} - p) \\ \frac{Dp_{\parallel}}{Dt} &= p_{\parallel} \left(\frac{D \ln B^{-2}n^3}{Dt} \right) - \nu_{coll}(p_{\parallel} - p) \end{aligned}$$

Subtracting these and setting the derivative of the pressure anisotropy to zero as prescribed by the Braginskii approximation, we obtain the Braginskii closure:

$$p_{\perp} - p_{\parallel} = \frac{3p}{\nu_{coll}} \frac{D}{Dt} \ln \frac{B}{n^{2/3}} = \frac{3p}{\nu_{coll}} \left(\hat{b}\hat{b} - \frac{\vec{\mathbb{I}}}{3} \right) : \nabla \vec{u} \quad (2.14)$$

The right hand side, the adiabatic invariance, produces the pressure anisotropy on the left hand side. One might conclude that, without collisions, anisotropy

is produced uncontrollably. This is however not true because the adiabatic invariants are no longer conserved once certain thresholds are reached [40].

The collisionless version of this closure, known as the double-adiabatic or Chew-Goldberger-Low (CGL) closure, was originally developed for fusion devices. We shall use the Braginskii formalism because of the many problems accrued by the CGL closure in astrophysical situations [40].

We can now write the MHD equations in terms of this closure. Some work yields:

$$\begin{aligned}
\frac{D \ln n}{Dt} &= -\nabla \cdot \vec{u} \\
\frac{D \ln B}{Dt} &= (\hat{b}\hat{b} - \mathbb{I}) : \nabla \vec{u} \\
\frac{3}{2}p \frac{D \ln pn^{-5/3}}{Dt} &= \frac{3p}{\nu_{coll}} \left[\left(\hat{b}\hat{b} - \frac{\mathbb{I}}{3} \right) : \nabla \vec{u} \right]^2 \\
mn \frac{D \vec{u}}{Dt} &= -\nabla \left(p_{\perp} + \frac{B^2}{8\pi} \right) + \frac{\vec{B} \cdot \nabla \vec{B}}{4\pi} + \nabla \cdot \left[\frac{3p}{\nu_{coll}} \left(\hat{b}\hat{b} - \frac{1}{3}\mathbb{I} \right)^2 : \nabla \vec{u} \right]
\end{aligned}$$

The right hand side of the entropy equation in the form of $|\nabla \vec{u}|^2$ represents viscous heating. Clearly, the viscous heating is anisotropic. But what does this mean? Examining the right hand side more closely, we see that the vector $\hat{b}\hat{b} - \mathbb{I}/3$ selects out the direction perpendicular to the magnetic field. Therefore, velocity gradients perpendicular to the magnetic field are wiped out by the dot product, whereas velocity gradients parallel to the magnetic field survive to be viscously damped. The same holds true for the momentum equation. We are led to conclude that there are no collisions across magnetic field lines, while there are collisions along magnetic field lines, leading to viscous momentum transport along field lines. Braginskii's ordering 2.11 forbids particles from moving across the field lines more than a distance of a mean free path. The situation is illustrated in Figure ??.

Extending this closure to the heat flux moment equation leads to anisotropic heat flux along field lines and then an instability due to entropy gradients known as the MagnetoThermal Instability (MTI), which has been studied both analytically and numerically for its applications to the ICM and winds in hot accretion flows [61–68]. A similar instability called the Heat-flux-driven Buoyancy Instability is also derived from relaxing the assumption that the magnetic field is perpendicular to temperature gradients [64, 69, 70].

2.1.5 Kinetic effects closure

There are several approaches to modifying the fluid equations to capture kinetic effects. Sharma et al. [42] has studied the transition from collisionless theory to MHD theory and found that the key difference is anisotropic collisions. This same anisotropy was present in the Braginskii MHD equations in the previous section. Braginskii MHD thus seems like an appropriate starting point off of which we can build in additional modifications to attempt to replicate kinetic effects.

Studies of kinetic theory over the years has shown that additional “parasitic” instabilities limit the growth of the pressure anisotropy [38, 71]. The three most important instabilities are the firehose, mirror, and ion cyclotron instabilities. The third will not be reproduced, as in Sharma et al. [71]. It is mostly relevant for plasmas with $\beta \lesssim 100$ whereas the present context of RIAFs has much higher β [41]. The first two instabilities, however, we can look at more closely.

As in outlined in numerous articles, a plasma with the pressure anisotropy

$$p_{\perp} - p_{\parallel} < -B^2/4\pi \quad (2.15)$$

is unstable to the firehose instability, and a plasma with pressure anisotropy

$$p_{\perp} - p_{\parallel} > B^2/8\pi \quad (2.16)$$

falls prey to the mirror instability [38, 71–73]. These instabilities are not collisions since the plasma is collisionless. They are rather Alfvén waves destabilized by the pressure anisotropy [71]. These waves tangle up the magnetic field of the plasma on the scale of the Larmor radius, which throws particles off of their trajectory. We can therefore model these instabilities as having an effective collision rate and thus a resistivity and viscosity [73, 74].

In light of the thresholds above, we manually cap the pressure anisotropy over the course of our simulations in Chapter 4. The hope is that such an anisotropy maximum will sufficiently capture the kinetic instabilities in a fluid closure, as discussed in Chapter 4.

2.2 Codes: Athena4.2 and Pegasus

The systems under consideration in this thesis are extremely complicated and thus require the use of simulations to model on large time or length

scales. Two codes are used for this purpose: one, an MHD solver, the other, a hybrid-kinetic particle-in-cell (PIC) code.

The code in use in Chapters 3 and 4 to simulate MHD systems is Athena4.2 (henceforth referred to as Athena). Athena, a response to the older code ZEUS, uses a higher-order Godunov scheme for flexibility and the constrained transport technique to ensure a divergence-free magnetic field. It is a highly-modularized grid-based code with additions such as adaptive mesh refinement (AMR) capabilities, special relativity, and dust [44, 75]. The shearing box approximation (as explained in Section 3.1.3) has also been implemented [45]. A new version of Athena, Athena++, more easily integrates general relativity and allows for better Riemannian solvers [76, 77].

For collisionless and weakly collisional plasmas, the distribution function itself must be evolved. Such evolution is accomplished with a so-called “particle-in-cell” or PIC code. Because a fully-kinetic code usually requires compromising assumptions such as reduced speed of light or a smaller ion-to-electron mass ratio, hybrid-kinetic codes such as PEGASUS, the one used in [38] that this thesis compares its results to in Chapter 4, are perhaps more useful. PEGASUS itself treats electrons as a massless fluid, while ions are treated kinetically. This assumption is valid since ions are much hotter than the efficiently-radiating electrons [18]. PEGASUS is a second-order accurate code that uses a three-stage predictor-predictor-corrector algorithm for integration. It also uses the constrained transport method as Athena does to enforce a divergence-less magnetic field and implements the shearing box method [72].

2.3 Early Problems in Accretion

The above sections have addressed the fundamental plasma physics behind radiatively-inefficient accretion flows and how they are implemented numerically. But how does accretion actually work on a fundamental level?

Accretion is the outward transport of angular momentum, which means that particles that lose angular momentum drop closer to the central accreting object (in the case of this thesis, a black hole) in accordance with differential rotation. The cause of this angular momentum transport is the real issue. It seems natural to explain this slowing down via friction; in an accretion disk, the matter at different radii are not moving at the same velocity (i.e.

there is a shear) and hence one might think that there is a sort of coefficient of kinetic friction between particles that slows down their movement and causes them to accrete. The idea that this “molecular” or “shear” viscosity could explain accretion rates is tempting, but in reality is not supported by simulations or observations.

Early simulations and observations showed accretion rates on the order of $10^{15} \text{ cm}^2/\text{s}$; however, the standard values of molecular viscosity are in the tens of cm^2/s , somewhere around 14 orders of magnitude too small [78]. This fantastic difference between theory and simulations resulted in several new ideas for explaining the transport of angular momentum and led to the formulation of one of the most well-known models for thin disks—the α -disk.

The seminal paper of Shakura and Sunyaev [79] explores accretion disks in the context of a binary star system. It essentially characterizes ignorance in the accretion rate via the parameter α , defining the tangential stress $w_{r\phi} = \alpha \rho v_s^2$, where v_s is the sound speed such that $\rho v_s^2/2$ is the disk matter’s thermal energy density, although definitions vary to order unity across sources [79]. This formulation temporarily removed the need to explain the source of the viscosity and provides a parameter that is easy to tweak in numerical simulations.

Despite its intuitive usefulness, the α prescription offers no mechanism for the transport of angular momentum. It was proposed that, while pure molecular viscosity could not explain the observed accretion rates, an “effective” viscosity due to eddy interaction could do the job [80]. In other words, turbulence would generate eddies whose interactions would manifest similar to a viscosity. The problem became to find the source of the turbulence that would lead to outward angular momentum transport. Supposing that an effective viscosity generated by turbulence can explain observed and simulated accretion rates, the question becomes: what causes this turbulence?

Some, influenced by laboratory fluid mechanics, believed that the sheer property of having a high Reynolds number (the product of a characteristic velocity and length scale divided by the viscosity; huge in astrophysical flows due to the large length scales involved) satisfactorily accounted for the needed turbulence. This allows for free energy to be extracted from the shear flow. However, Keplerian flows are stable against perturbations (i.e. experience no turbulence) where shear flows are not (given that the specific angular momentum increases outward—Rayleigh’s criterion). The differ-

ence is due to epicycles in Keplerian flows, which sink the energy that would otherwise devolve into prominent disturbances. A high Reynolds number is not enough to explain the necessary turbulence.

It was long thought (and indeed, is still under discussion) that hydrodynamic (mostly convective) instabilities could lead to turbulence in accretion disks [81, 82]. Other possibilities include non-local effects such as waves and shocks created by tidal forces. These effects can produce accretion at rates up to $\alpha = .01$, but only in hot disks [78]. Global disk winds, of the type suggested by Blandford and Znajek [83], could also transport angular momentum. These magnetically-driven winds could theoretically sweep matter around in such a way as to account for the high accretion rates without a viscosity while also helping account for AGN jets [84]; however, the presence of these winds in all accretion disks is debated. A more universal and fundamental explanation seems more likely.

Magnetic fields were thought to serve an amplifying role in turbulence transport. That is, with pre-existing turbulence, magnetic fields would tangle and speed along the transportation of magnetic fields [79]. It was thought that the magnetic pressure and pressure due to turbulence were distinct, and that magnetic pressure would be insignificant in disk situations, or would require large magnetic fields on the order of $10^7 - 10^8$ G to balance the gravitational pressure of infalling gas [80]. The magnetic field was mainly considered to be important due to consequences of cyclotron radiation as a cooling mechanism [85]. It was not until the early 1990s that the full significance of magnetic fields was appreciated.

In 1991, Balbus and Hawley [86–88] closed the conceptual circle by showing that turbulence resulted directly from a weak magnetic field. Pre-existing turbulence was not needed; the entire sequence of generating turbulence and transporting turbulence and angular momentum could be derived as a result of a linear instability in the MHD equations (see Section 3.1). Numerous numerical simulations have since confirmed the important role of magnetic fields in accretion processes. The next chapter will explore this linear instability in the context of numerical simulations 4.

Chapter 3

Computational Context Through the MRI

This chapter examines the solution to the problem of accretion mentioned in the last section of Chapter 2.3: the MagnetoRotational Instability (MRI). In doing so, it also presents intuition on how the magnetic field interacts in a rotating flow and how the MHD equations outlined in Chapter 2.1 actually manifest. Although some traction can be gained analytically (indeed, the instability itself arises from linear theory), this chapter will use simulations to illustrate the linear and nonlinear theory of the MRI and to introduce principles of using numerical simulations.

The MRI is fundamentally a local instability; as such, we will zoom in closely to look at a small patch of the overall accretion disk and examine the microphysics at work (see Figure 3.1). The local MHD equations as well as important characteristics such as which wavelengths grow the fastest (and how fast they grow) is outlined in Section 3.1. Non-ideal theory and simulations introduce important concepts such as numerical dissipation in Section 3.2.

3.1 Local Ideal MHD Theory and Simulations

In the local approximation, we consider an unperturbed patch of accretion disk with a Keplerian rotation profile at radius r_0 threaded by a uniform vertical magnetic field. On such small scales, the patch looks like a rectangular prism. We can write the equations in Cartesian form with the radial direction as x and the azimuthal direction as y . The Keplerian differential rota-

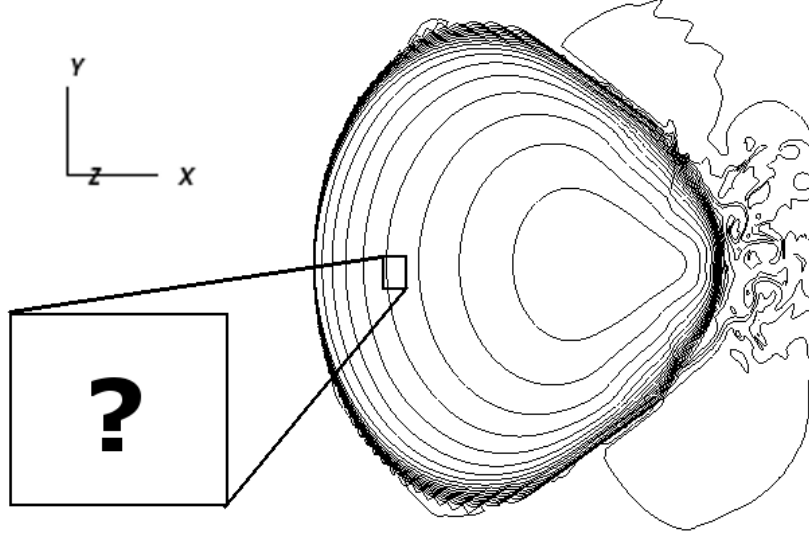


Figure 3.1: Global axisymmetric simulation of a hot accretion flow. Such simulations are expensive, so we zoom in to a small box (the “shearing box”, see Section 3.1.3) to look at the microphysics.

tion in this frame looks like a combination of background shear $\vec{u}_0 = 2A_0x\hat{y}$ where $A_0 = -3\Omega_0/4$ for Keplerian flow. The ideal MHD equations in this frame are:

$$\nabla \cdot \vec{u} = \nabla \cdot \vec{B} = 0 \quad (3.1)$$

$$\frac{\partial \vec{u}}{\partial t} = -\vec{u} \cdot \nabla \vec{u} - \frac{1}{\rho} \nabla P + \frac{1}{c\rho} \vec{J} \times \vec{B} - 2\Omega_0 \hat{z} \times \vec{u} - 4A_0\Omega_0 x \hat{x} \quad (3.2)$$

$$\frac{\partial \vec{B}}{\partial t} = \nabla \times (\vec{u} \times \vec{B}) \quad (3.3)$$

The second equation incorporates the Coriolis force $-2\Omega_0 \hat{z} \times \vec{u}$ and the background linear shear [89].

The ultimate goal here is to obtain a relationship between the frequency ω of a wave perturbation and its wavelength k . As such, we consider leading order plane-wave solutions (WKB disturbances) of the form

$$\vec{u} = 2A_0x\hat{y} + \delta\vec{u}e^{-i(\omega t - kz)} \quad (3.4)$$

$$\vec{B} = B_0\hat{z} + \delta\vec{B}e^{-i(\omega t - kz)} \quad (3.5)$$

This form of linear theory is the cornerstone of linear instability analysis in plasma physics and can be found in a number of references [69, 80, 86–89]. Plugging in this form and eliminating variables, we attain the dispersion relation

$$\omega^4 - \omega^2[\kappa^2 + 2(\vec{k} \cdot \vec{v}_A)^2] + (\vec{k} \cdot \vec{v}_A)^2 \left((\vec{k} \cdot \vec{v}_A)^2 + \frac{d\Omega^2}{d \ln R} \right) \quad (3.6)$$

where $\vec{v}_A = \vec{B}/\sqrt{4\pi\rho}$ is the Alfvén velocity. This equation is also in the Boussinesq limit that the sound speed goes to infinity, which filters out unimportant sound waves [80, 90].

3.1.1 Ideal MRI Condition for Stability and Maximum Growth Rate

From the dispersion relation Eq. 3.6, we can see the condition for stability (that is, real frequency) is

$$(\vec{k} \cdot \vec{v}_A)^2 > -\frac{d\Omega^2}{d \ln R} \quad (3.7)$$

It is interesting to note that it is always possible to find a wavenumber k such that the system is unstable unless $\frac{d\Omega^2}{d \ln R} > 0$, which would be very uncommon in astrophysical disks [80]. Thus the MRI is always present in weakly magnetized disks with a Keplerian rotation profile.

Also note that if the magnetic field $B = 0$, then the Alfvén velocity is also zero and Eq. 3.7 would have us believe that the hydrodynamic criterion for disk stability is $\frac{d\Omega^2}{d \ln R} > 0$. We know however that the Rayleigh linear stability criterion says that $4\Omega^2 + \frac{d\Omega^2}{d \ln R} > 0$. The disagreement is due to the assumptions made in using the MHD equations, namely, that the mean free path of particles was much less than the length scales of interest. As k increases, we get down to such small scales that the scales of interest become comparable to the mean free path and thus this assumption is no longer valid. The conflict must be resolved through kinetic theory. This is another incentive to see if we can get the MHD equations to somehow approximate kinetic theory in Chapter 4.

One of the most important questions for simulations is making sure that the wavelengths that are growing the fastest are resolved on the numerical grid. For this we need the wavelength of the fastest-growing mode.

The maximum unstable growth rate is given by taking the derivative of the dispersion relation with respect to frequency. From this we find that the largest growth rate ω_{max} is given by

$$|\omega_{max}| = \frac{1}{2} \left| \frac{d\Omega}{d \ln R} \right| = \frac{3}{4} \Omega \quad (3.8)$$

with the Keplerian values on the right. Plugging this back into the dispersion relation shows that the maximum growth rate occurs when

$$(\vec{k} \cdot \vec{v}_A)_{max}^2 = - \left(\frac{1}{4} + \frac{\kappa^2}{16\Omega^2} \right) \frac{d\Omega^2}{d \ln R} = \frac{\sqrt{15}}{4} \Omega \quad (3.9)$$

There are several interesting things to note here. First, the maximum growth rate is independent of the magnetic field strength. It is also very large and apparently can grow without bound (although as we will show later other instabilities keep it in check). In fact, Balbus and Hawley [91] suggest that this growth rate is the fastest possible for a linear instability that is powered by the free energy of differential rotation.

We can see this growth in action by examining Figure 3.2, which plots perturbations in azimuthal angular momentum. There is clearly a periodic structure which in the x-direction has a wavelength of about half of the box size. This is what we expect from Eq. 3.9:

$$(\vec{k}_{max} \cdot \vec{v}_A)^2 = k_{max}^2 \frac{B^2}{4\pi\rho} = \frac{k_{max}^2}{4\pi\rho} \frac{8\pi P}{\beta} = \frac{2P}{\beta\rho} k_{max}^2 = \frac{15}{16} \Omega^2$$

With the parameters of the simulation having been chosen to set $\Omega = 1$, $P/\rho = 1$, and $\beta = 400$, we have $k_{max} = 13.7 H^{-1}$ in units of the box size H . The wavelength λ_{max} of the fastest growing mode is then $\lambda_{max} = 2\pi/k_{max} = .46H$. The figure shows this and its orientation along the x-direction. The z-direction mode has a different growth rate and wavelength. In this simulation, the magnetic field is given as $\vec{B} = B_0 \sin\left(\frac{2\pi x}{H}\right) \hat{z}$. This choice is significant only in that it has zero net flux; the actual form as a sine wave is somewhat arbitrary as it is just a simple way to achieve the zero net flux condition.

More detailed analysis of the instability can be found in [86], henceforth referred to as BH1 and [80], henceforth referred to as BH2. The instability is different given different initial configurations of the magnetic field, the

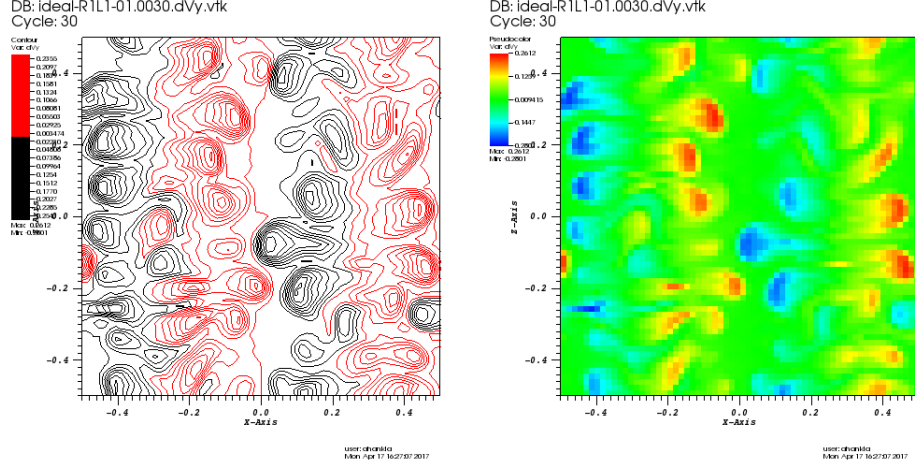


Figure 3.2: Slice at $t = 3.0$ orbits. Central body is on the left; z-direction is up. Left: Contour plot of angular momentum perturbations. Black is a perturbation in the negative y-direction, while red is in the positive y-direction. XX do this XX. Right: Pseudocolor plot of angular momentum perturbations. Plot is normalized to XX do this XX. The growth of the x-direction mode with wavelength $.5H$ is clear.

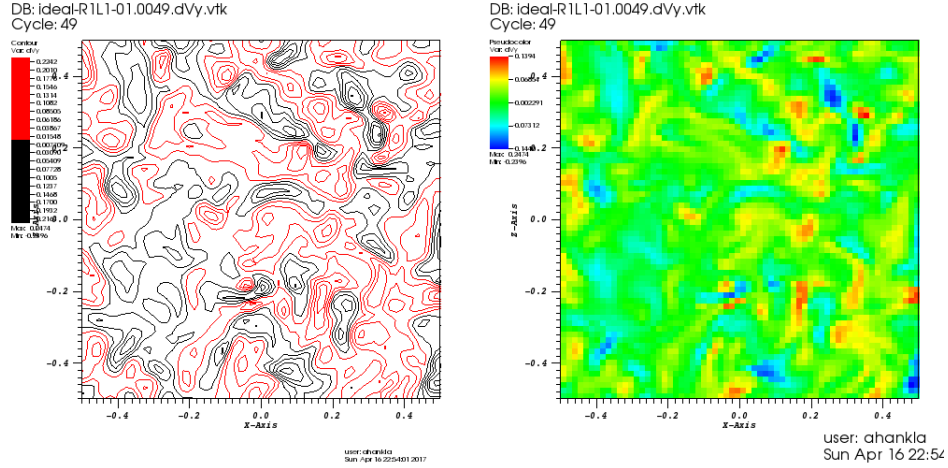


Figure 3.3: Slice at $t = 4.9$ orbits of angular momentum perturbations with same description as Fig. 3.2. The system has proceeded to the nonlinear turbulence phase as evidenced by the lack of structure.

most important being the aforementioned zero net-flux condition. A radial magnetic field component will yield a time-dependent azimuthal magnetic field component; however, this dependency does not really affect the MRI evolution because the axisymmetric instability is independent of B_ϕ [80].

We can see that the MRI is working because over time the magnetic energy and kinetic energy increase, shown in Figure 3.4. Some of the (in this case, unlimited) energy from differential rotation is going into turbulence, sustaining the magnetic field and churning around particles. The linear phase of the MRI in Figure 3.2 gives way to turbulence shortly thereafter, as shown in Figure 3.3. The nonlinear regime is the steady-state solution and is what we are most interested in for this thesis. This is the regime that is difficult to describe analytically. Note that references such as BH1 that perform two-dimensional calculations see the rise of a “channel mode” between the linear and nonlinear evolution. In three-dimensional calculations the channel mode breaks down much faster into turbulence [92, 93].

Details of the method used to produce Figures 3.2 and 3.4 are explained in Section 3.1.3.

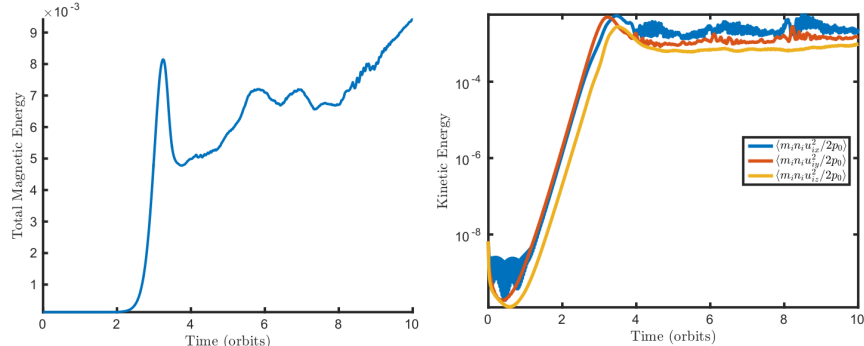


Figure 3.4: Left: Magnetic energy increases due to MRI turbulence. Total magnetic energy has been normalized to initial pressure. Right: Kinetic energy, also normalized to initial pressure. The large bump around $t = 3$ orbits is due to the channel mode (see text). Resolution is $(64, 128, 64)$ zones for the $(H, 4H, H)$ box.

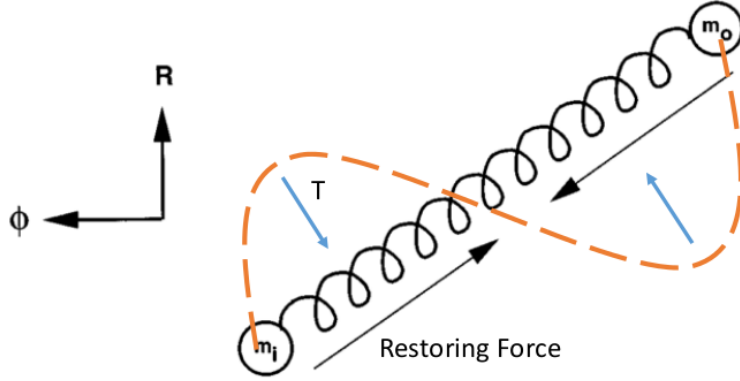


Figure 3.5: Illustration of the MRI with the magnetic tension T working in the same way as the restoring force of a spring. Adapted from BH2.

3.1.2 Spring Interpretation

It turns out that the local equations are also those of two orbiting masses coupled by a spring. A more complete derivation is given in BH2, so here we only provide the physical intuition for how the MRI leads to accretion.

The situation is illustrated in Figure 3.5. One mass (call it m_o) is orbiting at a slightly higher-radius orbit r_o thanks to a perturbation. Due to the Keplerian rotation law, this mass orbits slower than the mass m_i at lower radius r_i . This means that m_i pulls ahead of m_o , thus stretching the spring. Hooke's law exerts a force pulling the springs back together, causing the inner mass to lose angular momentum and the outer mass to gain angular momentum. This means that m_i drops down to a lower orbit while m_o pulls away, thereby stretching the spring even more. The process runs away and m_i falls inward while m_o falls outward, producing outward angular momentum transport.

Obviously there is not an actual spring connecting the two masses. The job of the spring's restoring force is done by magnetic tension $\left(\frac{1}{4\pi}(\vec{B} \cdot \nabla)\vec{B}\right)$, which tries to unfurl magnetic field lines. The magnetic field is perturbed when the fluid elements are due to the flux-freezing explained earlier. The field line is drawn as a dotted orange line in Figure 3.5.

3.1.3 Shearing Box Method

Simulations of the MRI are often achieved by solving the Cartesian set of MHD equations described above with periodic boundary conditions. The model's linear shear means that if a particle moves outward with radius, it also moves azimuthally. The boundary conditions for a function f are expressed as

$$f(x, y, z) = f(x + H_x, y + \frac{3}{2}\Omega_0 H_x t, z) \quad (3.10)$$

$$f(x, y, z) = f(x, y + H_y, z) \quad (3.11)$$

$$f(x, y, z) = f(x, y, z + H_z) \quad (3.12)$$

where the first line is for the x boundary, the second for the y boundary, and the third for the z boundary. The size of the computational regime is H_x in the x-direction, H_y in the y-direction, and H_z in the z-direction. In these equations the shear has been Taylor-expanded about the relative velocity $w_y = v_y - R\Omega_0 = R(\Omega - \Omega_0) \sim x \left(R \frac{d\Omega}{dR}\right)_0 = -\frac{3}{2}\Omega_0 x$ for a Keplerian disk. These boundary conditions are visually explained in Figure 3.6. More details can be found in BH2 or in the first paper simulating the MRI [88].

Since the box is in the local approximation, we can take the density and pressure to be initially constant. In this thesis, we evolve the system adiabatically as opposed to isothermally as discussed in Chapter 2.1.3. We also choose units such that the fiducial angular velocity of the shearing box as it goes around the central body is 1: $\Omega_0 = 1$. Also choosing $P = \rho = 1$, we have that the sound speed $c = 1$ and thus that the disk height $H = 1$.

Finally, note the importance of resolution: if the fastest growing MRI mode is smaller than the size of each zone, then the simulation will not resolve the mode and the set-up will appear stable. Calling the size of each zone $(\Delta x, \Delta y, \Delta z)$, the smallest resolvable wavelength in the x-direction is

$$\lambda_{min} = 2\Delta x$$

With a resolution of 64 zones per scale height H (the size of the entire computational regime), each zone has a size $\Delta x = 1/64 [H]$ so the smallest wavelength we can see corresponds to $\lambda_{min} = 1/32 [H] \approx .03 [H]$. We need the fastest growing wavelength to be bigger than this in order to see turbulence. This sets a limit on what β can be. We know that the fastest

growing wavelength is

$$\frac{15}{16}\Omega^2 = k_{fast}^2 v_A^2 = \frac{2(2\pi)^2}{\beta \lambda_{fast}^2}$$

$$\lambda_{fast}^2 = \frac{32(2\pi)^2}{15\beta}$$

Requiring that $\lambda_{fast} \geq \lambda_{min}$ yields an upper limit on β , which luckily is in the 10^4 range and thus well above the $\beta = 400$ case we are considering.

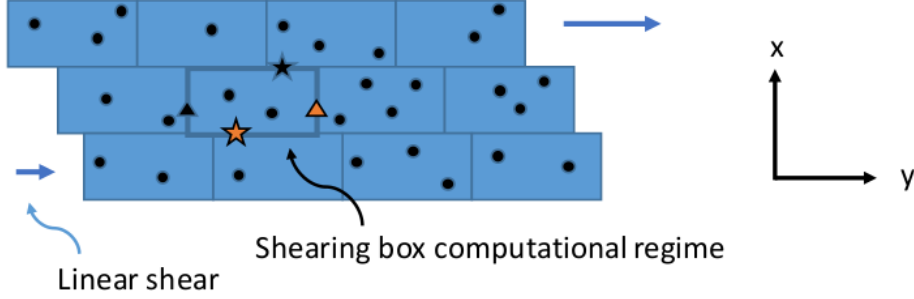


Figure 3.6: Illustration of the shearing box method. The computational regime itself is outlined in thick blue (“shearing box computational regime”) and has dimensions of $H_x = H$, $H_y = 4H$, and $H_z = H$ (z dimension not shown). The azimuthal direction needs a larger computational domain because the shear stretches the modes out. The linear shear $\vec{u}_0 = 2A_0 x \hat{y}$ is illustrated by arrows that vary in size with the x-location. The boundary conditions of Eqns. 3.10-3.12 are shown by the orange and black triangle and star. A particle that travels off the right (y) boundary (orange triangle) reappears on the left y boundary at the same x-position, represented by the black triangle. The x boundary condition takes into account the linear shear, such that the orange star leaving through the x boundary reappears displaced as though by a shear at the top of the regime (black star). Adapted from BH2.

3.2 Local Non-ideal MHD Theory and Simulations

This section is particularly relevant for the next chapter and understanding the effects of changing resistivity and viscosity in a fluid model. When we introduce non-ideal MHD components such as resistivity and viscosity, the

resolution of simulations becomes even more important. This is because certain length scales are damped faster than others. A problem in the literature involving the lack of convergence for zero net-flux simulations such as these was recently resolved [94, 95].

As a rough estimate, resistivity has a characteristic wavelength $k^2\eta \sim \Omega$ that is damped by $1/e$ over the time it takes for a sound wave to traverse the disk. Too big a value will damp the MRI and stabilize the disk [96]. Viscosity similarly damps wave numbers $k^2\nu \sim \Omega$. The balance between these two competing scales means that there is a limited parameter space in magnetic Prandtl number that can be explored. For example, sustaining turbulence requires $Pm \geq 4$ [57, 97] (the case is different for net-flux simulations [98]). The growth rate of resistive MHD is examined more rigorously in BH2.

However, the magnetic Reynolds number is also important, since if it is too small then numerical dissipation will dominate over physical dissipation and the magnetic Prandtl number will mean nothing. To figure out what regimes of the transport coefficients η and ν to look at, we must find values that are both physically meaningful and that do not overdamp the fastest growing modes (which would lead to stability).

We begin by requiring that the smallest resolvable wavelength be damped by physical resistivity: this sets

$$\eta \sim \frac{\lambda_{min}^2 \Omega}{(2\pi)^2} \gtrsim \frac{(1/32)^2}{(2\pi)^2} = 2.5e-5$$

For good measure we will take $\eta = 1e-4$ or above in our simulations. Also note that the value of η that corresponds to damping the fastest growing mode is

$$\eta_{fast} = \frac{1}{k_{fast}^2} \approx .005$$

With a resistivity lower than $5e-3$ we ensure that the MRI will still be able to grow.

A set of simulations with $\eta = 1e-4$ is shown in Figure 3.7a) with varying magnetic Prandtl number (Pm). We can see that magnetic energy increases with increasing Pm . However, Figure 3.7b) shows that increasing Pm does not lead to monotonically. To explain this, look at how the viscosity affects

the fastest growing mode. The characteristic viscously damped wavenumber k_ν is

$$k_\nu^2 = \frac{\Omega}{\nu} = \frac{\Omega}{\eta} \frac{\eta}{\nu} = k_\eta^2 \frac{1}{Pm}$$

For $\eta = 1e-4$, we have $k_\eta = 10^2$ and $k_\nu = \frac{1}{2}10^2 = 50$ for $Pm = 4$ or $k_\nu = \frac{1}{4}10^2 = 25$ for $Pm = 16$. However, for $\eta = 2e-4$, low Pm such as $Pm = 4$ gives $k_\nu = \frac{1}{\sqrt{8}}10^2 \approx 35$, but higher Pm like $Pm = 16$ gives $k_\nu = \frac{1}{\sqrt{32}}10^2 \approx 17$. The fastest growing mode is $k_{fast} \approx 14$, so for higher resistivities the higher Pm start to significantly damp modes that are most important to the MRI. In such cases, the flow will not be turbulent and so the magnetic energy will decay. A schematic portrayal of the scales involved is shown in Figure 3.8.

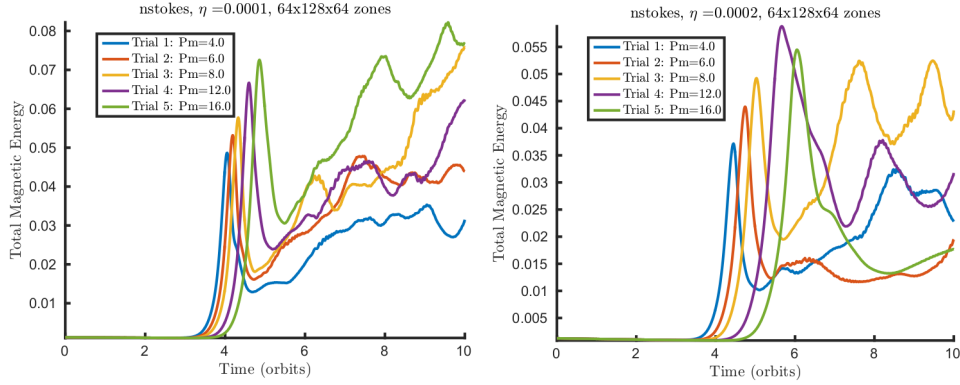


Figure 3.7: Plots of magnetic energy with increasing magnetic Prandtl number. The left panel has $\eta = 1e-4$ and the right has $\eta = 2e-4$. For the lower resistivity, magnetic energy increases monotonically up to $Pm = 16$. For a higher resistivity however, viscous damping begins to stabilize the MRI and higher Pm result in a decrease of magnetic energy.

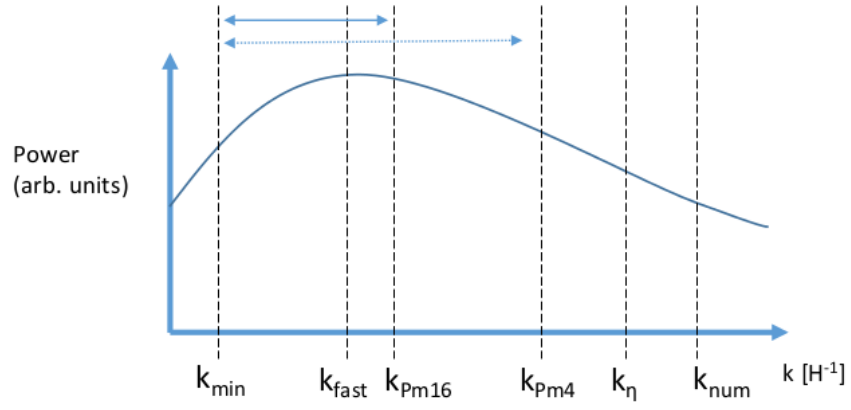


Figure 3.8: Rough illustration of scales involved in a shearing box simulation. The fastest-growing mode is labelled k_{fast} ; the lowest resolvable wavenumber has a wavelength twice the disk scale height and is labelled as k_{min} . Numerical dissipation cuts off wavenumbers above k_{num} , while resistivity damps wavenumbers above k_{η} . Two values for k_{ν} are shown, one for $Pm = 4$, the other for $Pm = 16$. Lower Pm resolve a wider range of wavenumbers than higher values, as shown by the horizontal arrows. Shape of power spectrum from the dispersion relation.

Chapter 4

Modified Fluid Closure of a Collisionless Plasma

This chapter puts together the pieces of the previous chapters in order to approximate a collisionless plasma with a modified fluid closure. Limiting the pressure anisotropy as explained in Chapter 2.1.5 is compared to simulations without a pressure cap.

4.1 Progress

Currently, I am establishing if the limiter is doing what I expect. Figure 4.1 shows runs with resistivity $\eta = 2 * 10^{-4}$ and the equivalent runs without the limiter in Figure 4.2. The limiters seem to reduce the effect of resistivity and magnetic Prandtl number, since as seen in Figure 4.3 and Figure 4.4, without the limiter there is wild variation.

The viscous stress is also greatly affected by the limiter; without it, viscous stress dominated the total stress as seen in Figure 4.5. With the limiter however, the viscous stress is negative (Figure 4.6). Why is this?

Looking at these trials in VisIt is also interesting: the linear evolution of the MRI seems to be quite different. Without the limiter I'm not sure I can find a linear growth stage; it just descends immediately into the channel mode (a double channel mode as compared to (**alias?**)) as shown in Figure 4.7. With the limiter, the instability takes longer to develop. Figure 4.8 shows a good view of the linear development, with the uncapped version shown for comparison to already have descended into the turbulent regime.

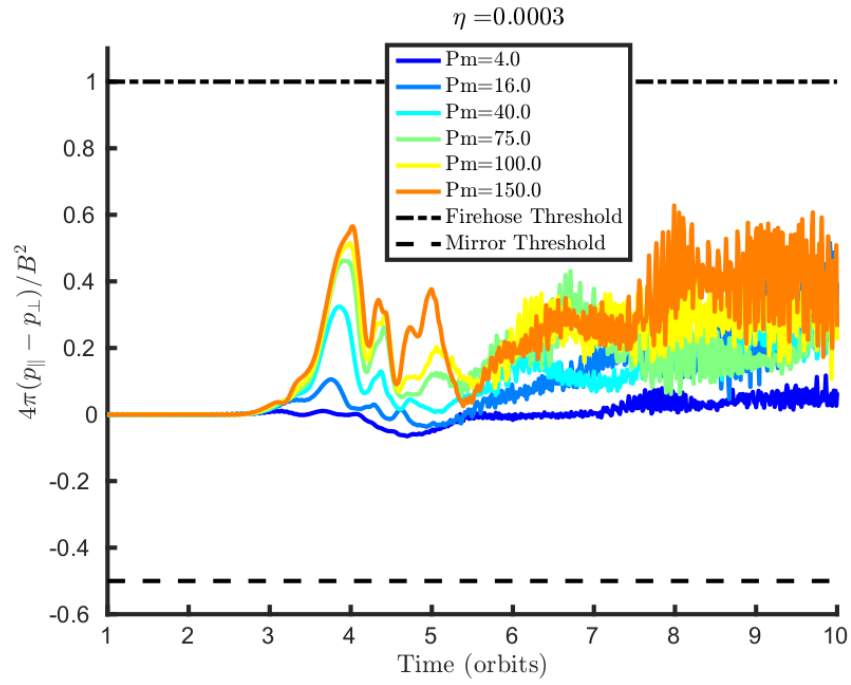


Figure 4.1: Simulations with $\eta = 3e-3$, scanning Pm . Anisotropy is capped, but never actually gets close to either threshold.

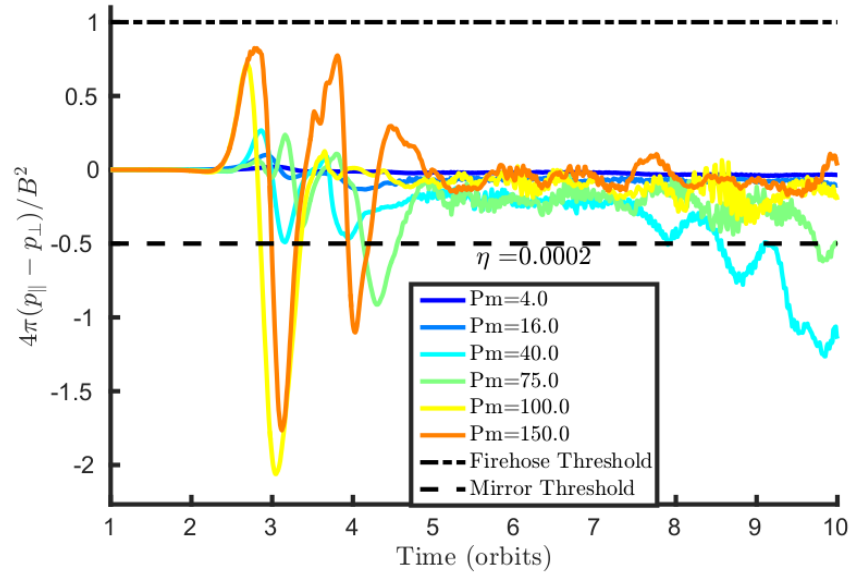


Figure 4.2: Simulations with $\eta = 2e - 3$, scanning Pm . Anisotropy is uncapped and greatly exceeds the mirror (but not the firehose) threshold.

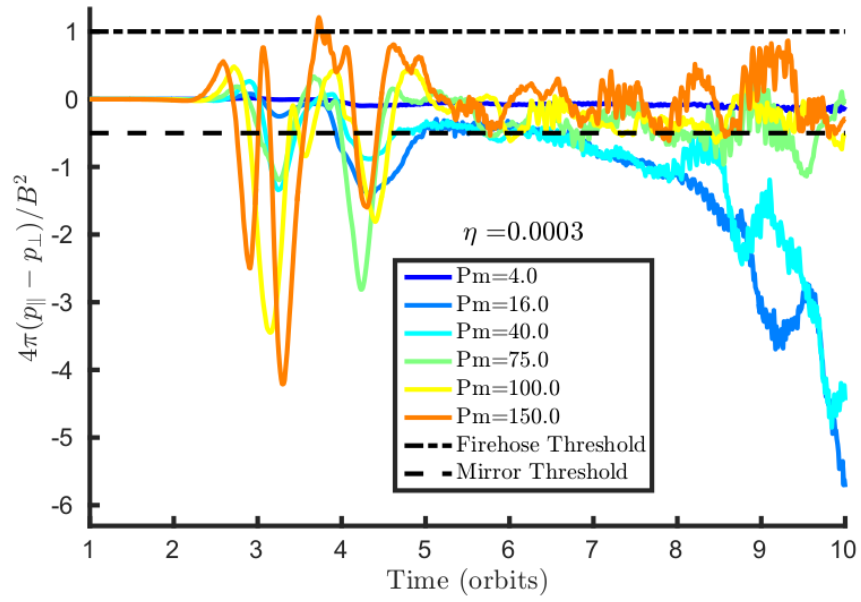


Figure 4.3: Simulations with $\eta = 3e - 3$, scanning Pm . Anisotropy is uncapped and exceeds both thresholds. Why do some Pm start to grow instead of oscillating?

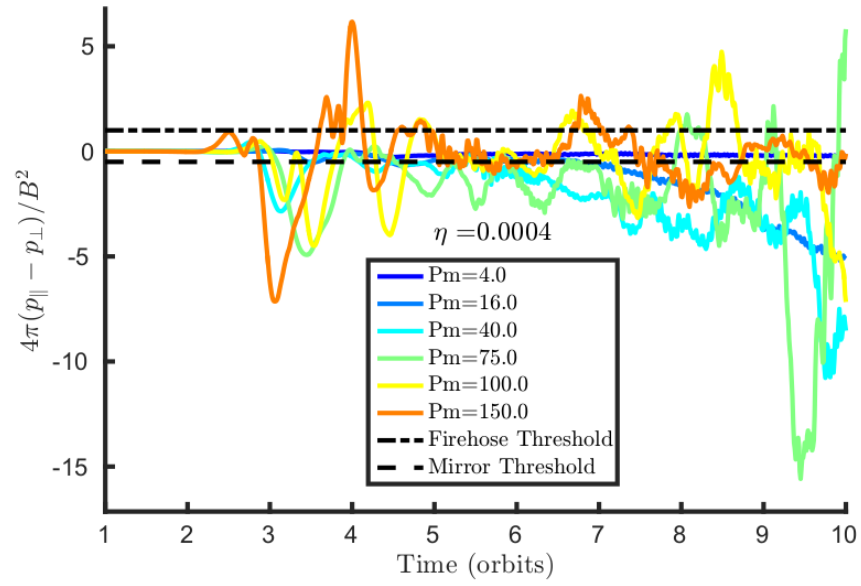


Figure 4.4: Simulations with $\eta = 4e - 3$, scanning Pm . Anisotropy is uncapped and mostly oscillatory...there is not a clear trend with increasing Pm .

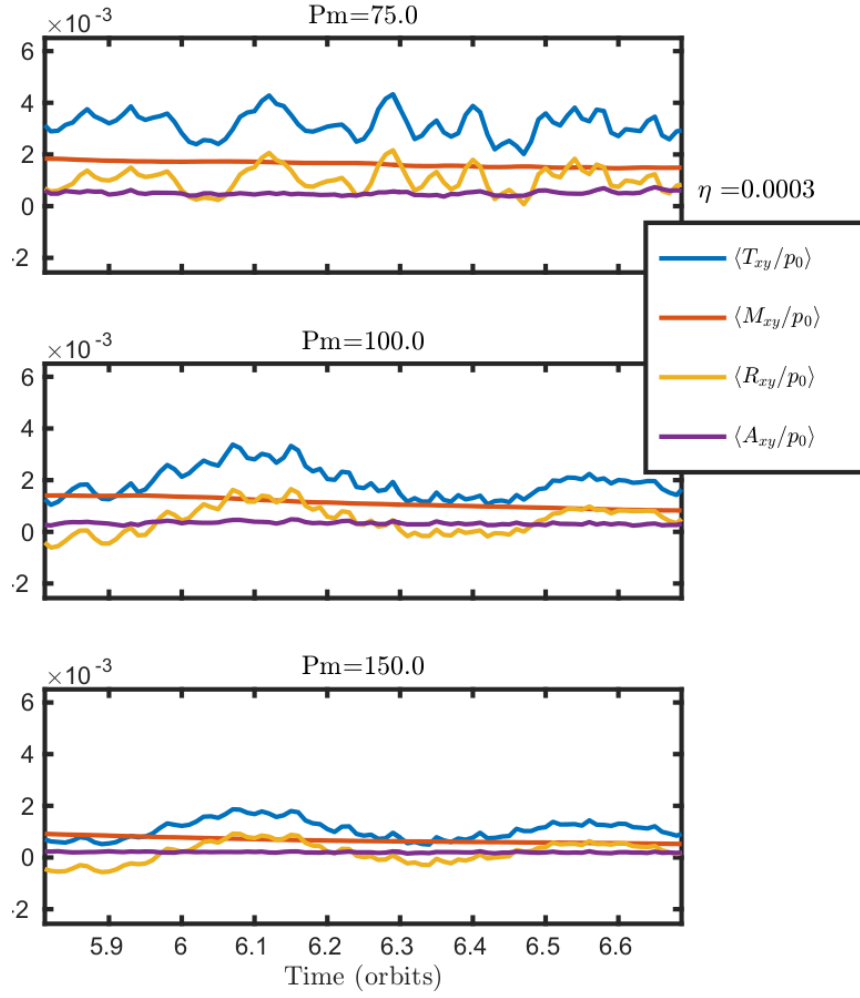


Figure 4.5: Viscous stress, uncapped. The negative viscous stress is plotted. Why is the Reynolds stress comparable to the Maxwell stress? And why is it sinusoidal?

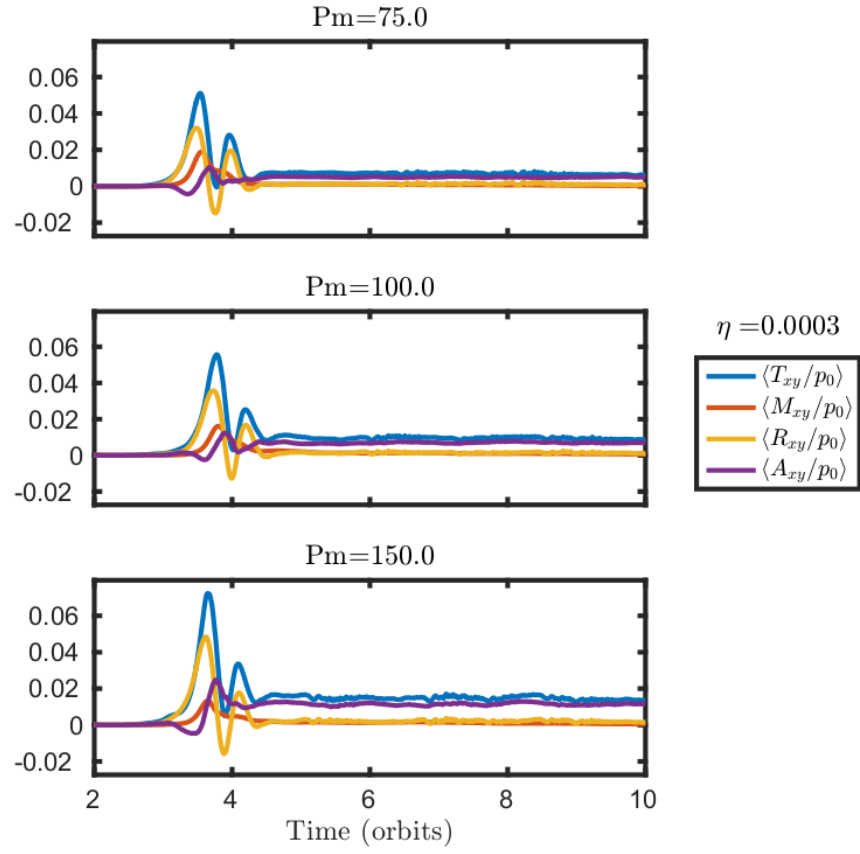


Figure 4.6: Viscous stress, capped. This is more normal and shows that the viscous stress is greatly exceeding the Maxwell and Reynolds stresses.

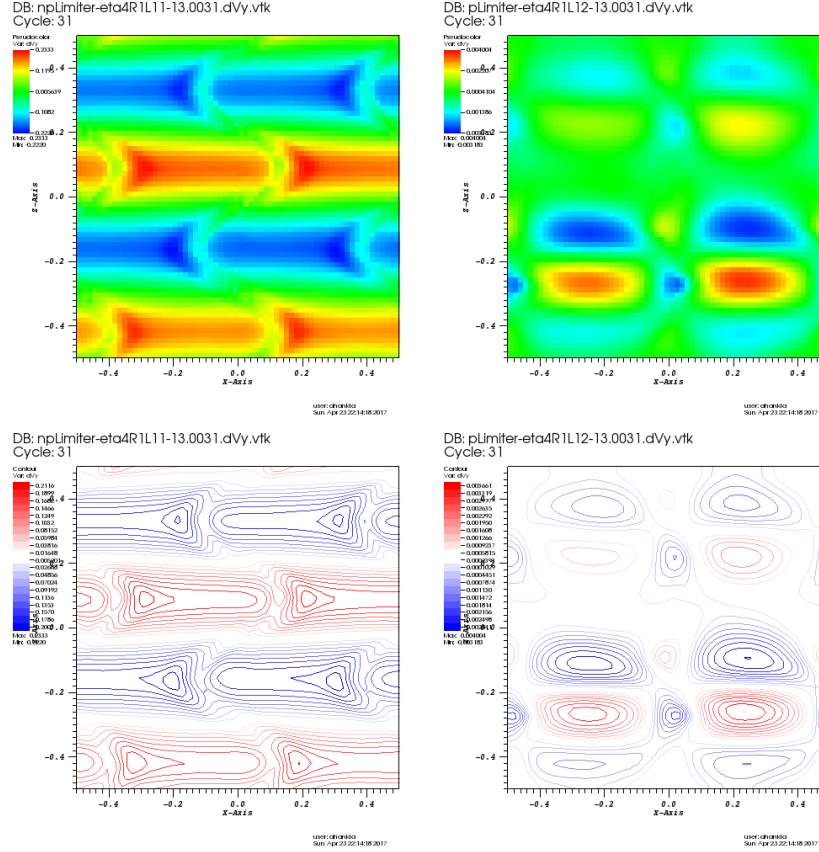


Figure 4.7: Azimuthal angular momentum perturbations, $t=3.1$ orbits. Left column: uncapped. Right column: capped. $\eta = 4e - 4$. Is this the channel mode on the left, and linear growth on the right?

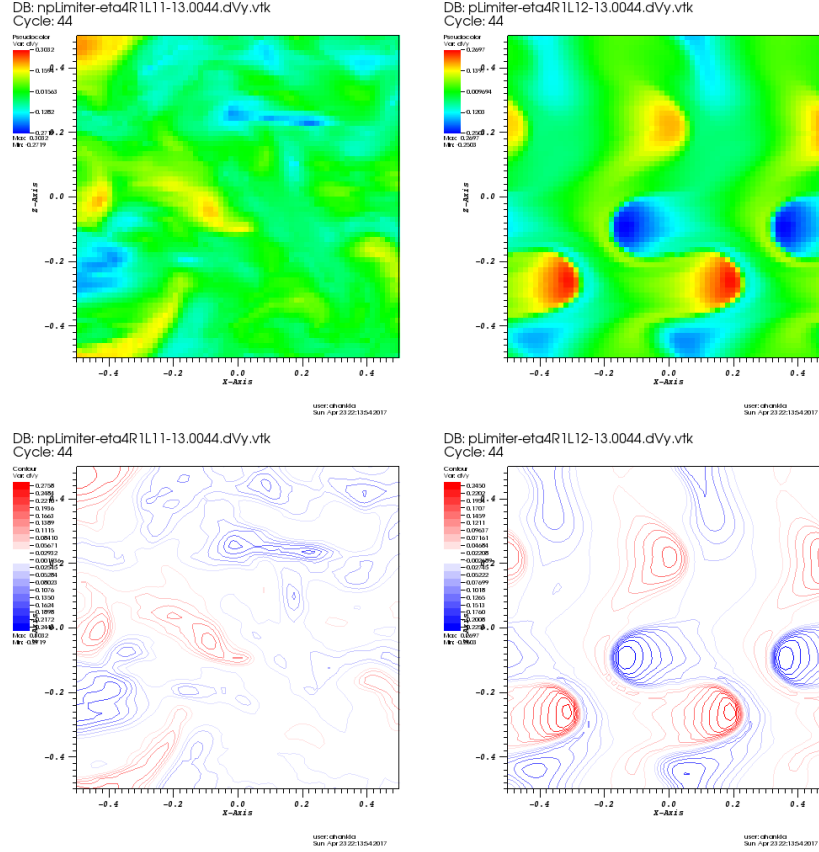


Figure 4.8: Azimuthal angular momentum perturbations, $t=4.4$ orbits. Left column: uncapped. Right column: capped. $\eta = 4e - 4$. Is this the channel mode on the right?

Bibliography

- [1] Avery E Broderick, Vincent L Fish, Sheperd S Doeleman, and Abraham Loeb. EVIDENCE FOR LOW BLACK HOLE SPIN AND PHYSICALLY MOTIVATED ACCRETION MODELS FROM MILLIMETER-VLBI OBSERVATIONS OF SAGITTARIUS A*. *Astrophys. J.*, 735(15pp), 2011. doi: 10.1088/0004-637X/735/2/110.
- [2] M L Goldstein, D A Roberts, and W H Matthaeus. MAGNETOHYDRODYNAMIC TURBULENCE IN THE SOLAR WIND. *Annu. Rev. Astron. Astrophys.*, 33:283–325, 1995. URL <http://www.annualreviews.org/doi/pdf/10.1146/annurev.aa.33.090195.001435>.
- [3] W. G. Pilipp, K.-H. Muehlhaeuser, H. Miggenrieder, M. D. Montgomery, and H. Rosenbauer. Characteristics of electron velocity distribution functions in the solar wind derived from the Helios plasma experiment. *J. Geophys. Res.*, 92(5):1075–1092, 1987. ISSN 0148-0227. doi: 10.1029/JA092iA02p01075.
- [4] M I Pudovkin and Andv S Semenov. MAGNETIC FIELD RECONNECTION THEORY AND THE SOLAR WIND -MAGNETOSPHERE INTERACTION: A REVIEW. *Sci. Rev.*, 41(1):1–89, 1985. URL <http://download.springer.com/static/pdf/528/art%7B%253A10.1007%7D%252FBF00241346.pdf?originUrl=http%7B%253A%7D%252Flink.springer.com%7D%252Farticle%7B%252F10.1007%7D%252FBF00241346%7D%252Ftoken2=exp=1492120748%7D%252Fstatic%7D%252Fpdf%7D%252F528%7D%252Fart%7D%2525253A10.1007%7D%2525252FBF00241346.pdf%7D%253ForiginUrl%7D%253>.
- [5] A. Fabian. COOLING FLOWS IN CLUSTERS OF GALAXIES. *Annu. Rev. Astron. Astrophys.*, 32:277–318, 1994. URL <http://www.annualreviews.org/doi/pdf/10.1146/annurev.aa.32.090194.001425>.
- [6] C L Carilli and G B Taylor. CLUSTER MAGNETIC FIELDS. *Annu. Rev. Astron. Astrophys.*, 40:319–48, 2002. doi: 10.1146/annurev.astro.40.060401.093852. URL <http://annualreviews.org/doi/pdf/10.1146/annurev.astro.40.060401.093852>.
- [7] P J Mendygral, T W Jones, and K Dolag. MHD SIMULATIONS OF ACTIVE GALACTIC NUCLEUS JETS IN A DYNAMIC GALAXY CLUSTER MEDIUM. *Astrophys. J.*, 750(17pp), 2012. doi: 10.1088/0004-637X/750/2/166. URL <http://iopscience.iop.org/article/10.1088/0004-637X/750/2/166/pdf>.
- [8] Matthew Kunz. press-Firehose and Mirror Instabilities in a Collisionless Shearing Plasma. 2010.
- [9] Jason Dexter and P Chris Fragile. Tilted black hole accretion disc models of Sagittarius A*: time-variable millimetre to near-infrared emission. *MNRAS*, 432:2252–2272, 2013. doi: 10.1093/mnras/stt583.
- [10] John F Hawley, Steven A Balbus, and James M Stone. A Magnetohydrodynamic Nonradiative Accretion Flow in Three Dimensions. *Astrophys. J. Lett.*, 554(1):49–52, 2001. ISSN 0004637X. doi: 10.1086/320931. URL <http://iopscience.iop.org/1538-4357/554/1/L49%7D%5Cnpapers2://publication/uuid/2C3A60D4-41E8-4DE1-B690-3CB8AF0B7406%7D%5Cnhttp://stacks.iop.org/1538-4357/554/i=1/a=L49>.
- [11] James M. Stone, John F. Hawley, Charles F. Gammie, and Steven A. Balbus. Three-dimensional Magnetohydrodynamical Simulations of Vertically Stratified Accretion Disks. *Astrophys. J.*, 463(2):656, 1996. ISSN 0004-637X. doi: 10.1086/177280. URL <http://adsabs.harvard.edu/cgi-bin/nph-data%7B%5D%7D%252Fquery?bibcode=1996ApJ...463..656S%7D%252Flink%7D%252Ftype=ABSTRACT%7D%5Cnpapers2://publication/doi/10.1086/177280%7D%5Cnhttp://adsabs.harvard.edu/doi/10.1086/177280>.
- [12] Yan-Fei Jiang, James M. Stone, and Shane W. Davis. ON THE THERMAL STABILITY OF RADIATION-DOMINATED ACCRETION DISKS. *Astrophys. J.*, 778(1):65, nov 2013. ISSN 0004-637X. doi: 10.1088/0004-637X/778/1/65.
- [13] Yan-Fei Jiang, James M. Stone, and Shane W. Davis. a Global Three-Dimensional Radiation Magneto-Hydrodynamic Simulation of Super-Eddington Accretion Disks. *Astrophys. J.*, 796(2):106, 2014. ISSN 1538-4357. doi: 10.1088/0004-637X/796/2/106. URL <http://stacks.iop.org/0004-637X/796/i=2/a=106?key=crossref.3345a0b680e6eb3d7be5065544be0d95>.

- [14] James; Stone and Michael Norman. Numerical Simulations of Magnetic Accretion Disks. *Astrophys. J.*, 433: 746–756, 1994.
- [15] N J Turner, J M Stone, and T Sano. Local Axisymmetric Simulations of Magnetorotational Instability in Radiation-dominated Accretion Disks. *Astrophys. J.*, 566(1):148–163, 2002. ISSN 0004-637X. doi: 10.1086/338081.
- [16] T Sano, S-I. Inutsuka, N J Turner, and J M Stone. Angular momentum transport by MHD turbulence in accretion disks: Gas pressure dependence of the saturation level of the magnetorotational instability. *Astrophys. J.*, 605:321–339, 2004.
- [17] Ronald A Remillard and Jeffrey E McClintock. X-ray Properties of Black-Hole Binaries. *Annu. Rev. Astron. Astrophys.*, 44:49–92, 2006.
- [18] Upasana Das and Prateek Sharma. Radiatively inefficient accretion flow simulations with cooling: implications for black hole transients. *MNRAS*, 435:2431–2444, 2013. doi: 10.1093/mnras/stt1452.
- [19] Upasana Das and Prateek Sharma. Cooling and black hole disk transitions. *ASI Conf. Ser.*, 8:27–30, 2013.
- [20] Andrzej Niedzwiecki, Fu-Guo Xie, and Agnieszka Stpnik. X-ray spectra of hot accretion flows. *MNRAS*, 443:1733–1747, 2014. doi: 10.1093/mnras/stu1262.
- [21] Aleksander Sadowski, Maciek Wielgus, Ramesh Narayan, David Abarca, and Jonathan C McKinney. Radiative, two-temperature simulations of low luminosity black hole accretion flows in general relativity. *MNRAS*, 000(0000):0–0, 2016.
- [22] Alexandra Veledina, Juri Poutanen, and Indrek Vurm. Hot accretion flow in black hole binaries: A link connecting X-rays to the infrared. *Mon. Not. R. Astron. Soc.*, 430(4):3196–3212, 2013. ISSN 00358711. doi: 10.1093/mnras/stt124.
- [23] R.P. Fender, J. Homan, and T.M. Belloni. Jets from black hole X-ray binaries: testing, refining and extending empirical models for the coupling to X-rays. *Mon. Not. R. Astron. Soc.*, 396:1370–1382, 2009.
- [24] Chris Nixon and Greg Salvesen. A physical model for state transitions in black hole X-ray binaries. *Mon. Not. R. Astron. Soc.*, 437(4):3994–3999, 2014. ISSN 00358711. doi: 10.1093/mnras/stt2215.
- [25] John F Hawley, Christian Fendt, Martin Hardcastle, Elena Nokhrina, and Alexander Tchekhovskoy. Disks and Jets Gravity, Rotation and Magnetic Fields. *Sp. Sci. Rev.*, 191:441–469, 2015. doi: 10.1007/s11214-015-0174-7. URL <http://download.springer.com/static/pdf/328/art%7B%7D253A10.1007%7D252Fs11214-015-0174-7.pdf?originUrl=http%7B%7D3A%7D2F%7D2Flink.springer.com%7D2Farticle%7D2F10.1007%7D2Fs11214-015-0174-7%7D&token2=exp=1492185262%7D~acl=%7D2Fstatic%7D2Fpdf%7D2F328%7D2Fart%7D25253A10.1007%7D25252Fs11214-015-0174-7.pdf>.
- [26] S M Ressler, A Tchekhovskoy, E Quataert, M Chandra, and C F Gammie. Electron thermodynamics in GRMHD simulations of low-luminosity black hole accretion. *MNRAS*, 454:1848–1870, 2015. doi: 10.1093/mnras/stv2084.
- [27] Feryal Oezel and Tiziana Di Matteo. X-Ray Images of Hot Accretion Flows. *Astrophys. J.*, 548:213–218, 2001.
- [28] Francois Foucart, Mani Chandra, Charles F. Gammie, and Eliot Quataert. Evolution of accretion discs around a kerr black hole using extended magnetohydrodynamics. *Mon. Not. R. Astron. Soc.*, 456(2):1332–1345, 2015. ISSN 13652966. doi: 10.1093/mnras/stv2687.
- [29] Avery E Broderick, Ramesh Narayan, John Kormendy, Eric S Perlman, Marcia J Rieke, and Sheperd S Doleman. THE EVENT HORIZON OF M87. *Astrophys. J.*, 805:179, 2015. doi: 10.1088/0004-637X/805/2/179.
- [30] D S Plant, R P Fender, G Ponti, T Muñoz-Darias, and M Coriat. Revealing accretion on to black holes: X-ray reflection throughout three outbursts of GX 339-4. *MNRAS*, 442:1767–1785, 2014. doi: 10.1093/mnras/stu867.
- [31] Ramesh Rohan, Jonathan E Narayan, M Ahadevan, G Rindlay, Robert G And, Charles Popham, and G Ammie. ADVECTION-DOMINATED ACCRETION MODEL OF SAGITTARIUS A* : EVIDENCE FOR A BLACK HOLE AT THE GALACTIC CENTER. *Astrophys. J.*, 492:554–568, 1998. URL <http://iopscience.iop.org/article/10.1086/305070/pdf>.
- [32] Avery E Broderick, Vincent L Fish, Sheperd S Doleman, and Abraham Loeb. ESTIMATING THE PARAMETERS OF SAGITTARIUS A*’s ACCRETION FLOW VIA MILLIMETER VLBI. *Astrophys. J.*, 697: 45–54, 2009. doi: 10.1088/0004-637X/697/1/45. URL <http://iopscience.iop.org/article/10.1088/0004-637X/697/1/45/pdf>.

- [33] Feng Yuan, Eliot Quataert, and Ramesh Narayan. NONTHERMAL ELECTRONS IN RADIATIVELY INEFFICIENT ACCRETION FLOW MODELS OF SAGITTARIUS A*. *Astrophys. J.*, 598:301–312, 2003.
- [34] S Doeleman, Eric Agol, Fred C Baganoff Geoffrey Bower, Avery Broderick Andrew Fabian, Paul Ho Mareki Honma Thomas Krichbaum Avi Loeb Dan Marrone NRAO, U Chicago Mark Reid Alan Rogers, Irwin Shapiro Peter Strittmatter Remo Tilanus Jonathan Weintroub Alan Whitney, and Melvyn Wright. Imaging an Event Horizon: submm-VLBI of a Super Massive Black Hole. *astro 2010 Decad. Rev. Comm.*, 2009.
- [35] A. Siemiginowska and M. Weiss. GB1508+5714: Most Distant X-ray Jet yet Discovered, 2003. URL <http://chandra.harvard.edu/photo/2003/gb1508/>.
- [36] J.P. Luminet. Black Hole Imaging (2): Heads and Tails, 2015. URL <http://blogs.futura-sciences.com/e-luminet/tag/accretion-disk/>.
- [37] J. Stone, M. Kunz, and A. Bhattacharjee. AST 521 Problem Set 1, 2016.
- [38] Matthew W Kunz, James M Stone, and Eliot Quataert. Magnetorotational Turbulence and Dynamo in a Collisionless Plasma. *Phys. Rev. Lett.*, 117, 2016. doi: 10.1103/PhysRevLett.117.235101.
- [39] P. Sharma, G. Hammett, and E. Quataert. Collisional Effects on the Kinetic MRI. *ASP Conf. Ser.*, 311: 139–140, 2004.
- [40] Prateek Sharma, Gregory W Hammett, Eliot Quataert, and James M Stone. SHEARING BOX SIMULATIONS OF THE MRI IN A COLLISIONLESS PLASMA. *Astrophys. J.*, 637:952–967, 2006.
- [41] Prateek Sharma, Eliot Quataert, Gregory W Hammett, and James M Stone. ELECTRON HEATING IN HOT ACCRETION FLOWS. *Astrophys. J.*, 667:714–723, 2007. URL <http://iopscience.iop.org/article/10.1086/520800/pdf>.
- [42] P. Sharma, G. Hammett, and E. Quataert. Transition from Collisionless to collisional magnetorotational instability. *Astrophys. J.*, 596:1121–1130, 2003.
- [43] Prateek Sharma. Kinetic Effects on Turbulence Driven by the Magnetorotational Instability in Black Hole Accretion. *PhD Thesis, 2007*, (September), 2007.
- [44] J. M. Stone, T. a. Gardiner, P. Teuben, J. F. Hawley, and J. B. Simon. Athena: A New Code for Astrophysical MHD. *Astrophys. J. Suppl. Ser.*, 178:137–177, 2008. ISSN 0067-0049. doi: 10.1086/588755. URL <http://arxiv.org/abs/0804.0402>.
- [45] James M Stone and Thomas A Gardiner. IMPLEMENTATION OF THE SHEARING BOX APPROXIMATION IN ATHENA. *Astrophys. J. Suppl. Ser.*, 189:142–155, 2010. doi: 10.1088/0067-0049/189/1/142.
- [46] Monika Moscibrodzka, Heino Falcke, Hotaka Shiokawa, and Charles F. Gammie. Observational appearance of inefficient accretion flows and jets in 3D GRMHD simulations: Application to Sagittarius A*. *Astron. Astrophys.*, 570, 2014. ISSN 0004-6361. doi: 10.1051/0004-6361/201424358.
- [47] Hotaka Shiokawa. General Relativistic MHD Simulations of Black Hole Accretion Disks: Dynamics and Radiative Properties, 2013.
- [48] Ramesh Narayan, Rohan Mahadevan, Jonathan E Grindlay, Robert Popham, and Charles Gammie. ADVECTION-DOMINATED ACCRETION MODEL OF SAGITTARIUS A* : EVIDENCE FOR A BLACK HOLE AT THE GALACTIC CENTER. *Astrophys. J.*, 492:554–568, 1998.
- [49] Charles F Gammie, Jonathan C Mckinney, Gá Bor, and Tó Th. HARM: A NUMERICAL SCHEME FOR GENERAL RELATIVISTIC MAGNETOHYDRODYNAMICS. *Astrophys. J.*, 589:444–457, 2003. URL <http://iopscience.iop.org/article/10.1086/374594/pdf>.
- [50] Scott C Noble, Charles F Gammie, Jonathan C Mckinney, and Luca Del Zanna. PRIMITIVE VARIABLE SOLVERS FOR CONSERVATIVE GENERAL RELATIVISTIC MAGNETOHYDRODYNAMICS. *Astrophys. J.*, 641:626–637, 2006. URL <http://iopscience.iop.org/article/10.1086/500349/pdf>.
- [51] Scott C Noble, Julian H Krolik, and John F Hawley. DIRECT CALCULATION OF THE RADIATIVE EFFICIENCY OF AN ACCRETION DISK AROUND A BLACK HOLE. *Astrophys. J.*, 692:411–421, 2009. doi: 10.1088/0004-637X/692/1/411. URL <http://iopscience.iop.org/article/10.1088/0004-637X/692/1/411/pdf>.
- [52] Chi-Kwan Chan, Dimitrios Psaltis, Ferya Öz, Ramesh Narayan, and Aleksander Adowski. THE POWER OF IMAGING: CONSTRAINING THE PLASMA PROPERTIES OF GRMHD SIMULATIONS USING EHT OBSERVATIONS OF Sgr A *. *Astrophys. J.*, 799(114pp), 2015. doi: 10.1088/0004-637X/799/1/1.
- [53] Monika Mocibrodzka, Charles F Gammie, Joshua C Dolence, Hotaka Shiokawa, and Po Kin Leung. RADIATIVE MODELS OF SGR A* FROM GRMHD SIMULATIONS. *Astrophys. J.*, 706:497–507, 2009. doi: 10.1088/0004-637X/706/1/497.

- [54] G Janeschitz, P Barabaschi, G Federici, M Shimada, D J Campbell, V Mukhovatov, R Aymar, V A Chuyanov, M Huguet, and Y Shimomura. Overview of ITER-FEAT -The future international burning plasma experiment The requirements of a next step large steady state tokamak Chapter 1: Overview and summary Overview of ITER-FEAT — The future international burning plasma experiment. *Nucl. Fusion*, 41:1301–1310, 2001. URL <http://iopscience.iop.org/0029-5515/41/10/301>.
- [55] G Grieger and I Milch. {D} as {F}usionsexperiment {WENDELSTEIN} 7-{X}. *Phys. Bl{\a}tter*, 49(11): 1001, 1993.
- [56] R. D. (Richard D.) Hazeltine and F. Waelbroeck. *The framework of plasma physics*. Perseus Books, Reading, 2004. ISBN 9780813342139.
- [57] S Fromang, J Papaloizou, G Lesur, and T Heinemann. MHD simulations of the magnetorotational instability in a shearing box with zero net flux II. The effect of transport coefficients. *A&A*, 476:1123–1132, 2007. doi: 10.1051/0004-6361/20077943.
- [58] G Lesur and P.-Y Longaretti. Impact of dimensionless numbers on the efficiency of magnetorotational instability induced turbulent transport. *Mon. Not. R. Astron. Soc.*, 378:1471–1480, 2007. doi: 10.1111/j.1365-2966.2007.11888.x.
- [59] C. Gammie. Layered Accretion in T Tauri Disks. *Astrophys. J.*, 457:355–362, 1996. URL http://articles.adsabs.harvard.edu/cgi-bin/nph-iarticle_query?1996ApJ...457..355G&defaultprint=YES&filetype=.pdf.
- [60] Claudia Negulescu and Stefan Possanner. CLOSURE OF THE STRONGLY MAGNETIZED ELECTRON FLUID EQUATIONS IN THE ADIABATIC REGIME. *MULTISCALE Model. SIMUL. c 2016 EUROfusion Consort.*, 14(2):839–873, 2016. doi: 10.1137/15M1027309.
- [61] M. Kunz. Braginskii-MHD and application to ICM, 2016.
- [62] Steven a. Balbus. Stability, Instability, and “Backward” Transport in Stratified Fluids. *Astrophys. J.*, 534(1):420–427, 2000. ISSN 0004-637X. doi: 10.1086/308732.
- [63] S. a. Balbus. Convective and Rotational Stability of a Dilute Plasma. *Astrophys. J.*, 562(2):909–917, 2001. ISSN 0004-637X. doi: 10.1086/323875. URL <http://arxiv.org/abs/astro-ph/0106283>.
- [64] Matthew W Kunz. Dynamical stability of a thermally stratified intracluster medium with anisotropic momentum and heat transport. *Mon. Not. R. Astron. Soc.*, 417:602–616, 2011. doi: 10.1111/j.1365-2966.2011.19303.x.
- [65] Ian J. Parrish and James M. Stone. Simulation of the magnetothermal instability. *Astrophys. Space Sci.*, 307(1-3):77–82, 2007. ISSN 0004640X. doi: 10.1007/s10509-006-9243-4.
- [66] Ian J. Parrish and James M. Stone. Nonlinear Evolution of the Magnetothermal Instability in Two Dimensions. *Astrophys. J.*, 633:334–348, 2005. ISSN 0004-637X. doi: 10.1086/518881. URL <http://arxiv.org/abs/astro-ph/0612195>.
- [67] Bryan M. Johnson and Eliot Quataert. The Effects of Thermal Conduction on Radiatively Inefficient Accretion Flows. *Astrophys. J.*, 660(2):1273–1281, 2007. ISSN 0004-637X. doi: 10.1086/513065.
- [68] De Fu Bu, Mao Chun Wu, and Ye Fei Yuan. Effects of anisotropic thermal conduction on wind properties in hot accretion flow. *Mon. Not. R. Astron. Soc.*, 459(1):746–753, 2016. ISSN 13652966. doi: 10.1093/mnras/stw723.
- [69] E. Quataert. Buoyancy Instabilities in Weakly Magnetized Low Collisionality Plasmas. *Astrophys. J.*, 673(2):758–762, 2008. ISSN 0004-637X. doi: 10.1086/525248. URL <http://arxiv.org/abs/0710.5521>.
- [70] I. Parrish and E. Quataert. NONLINEAR SIMULATIONS OF THE HEAT-FLUX-DRIVEN BUOYANCY INSTABILITY AND ITS IMPLICATIONS FOR GALAXY CLUSTERS. *Astrophys. J.*, 677:9–12, 2008.
- [71] P. Sharma, E. Quataert, and J. M. Stone. Spherical accretion with anisotropic thermal conduction. *Mon. Not. R. Astron. Soc.*, 389(4):1815–1827, 2008. ISSN 00358711. doi: 10.1111/j.1365-2966.2008.13686.x.
- [72] Matthew W Kunz, James M Stone, and Xue-Ning Bai. Pegasus: A new hybrid-kinetic particle-in-cell code for astrophysical plasma dynamics. *J. Comput. Phys.*, 259:154–174, 2014. doi: 10.1016/j.jcp.2013.11.035.
- [73] A A Schekochihin, S C Cowley, R M Kulsrud, M S Rosin, and T Heinemann. Nonlinear Growth of Firehose and Mirror Fluctuations in Astrophysical Plasmas. *Phys. Rev. Lett.*, 100, 2008. doi: 10.1103/PhysRevLett.100.081301. URL <https://journals.aps.org/prl/pdf/10.1103/PhysRevLett.100.081301>.
- [74] M. Kunz. Private Communication, 2017.

- [75] James M Stone. The Athena MHD Code: Extensions, Applications, and Comparisons to ZEUS. *ASP Conf. Ser.*, 406:277–286, 2009. URL <http://articles.adsabs.harvard.edu/cgi-bin/nph-iarticle?dbkey=AST&bibcode=2009ASPC...406..277S&letter=0&classic=YES&defaultprint=YES&whole=&paper=YES&page=277&epage=277&send=Send+PDF&filetype=.pdf>.
- [76] C. White and J. Stone. *Development and application of numerical techniques for general-relativistic magnetohydrodynamics simulations of black hole accretion*. - Princeton University Library Catalog. PhD thesis, Princeton University, 2016. URL <https://pulsesearch.princeton.edu/catalog/10096882>.
- [77] Christopher J White, James M Stone, and Charles F Gammie. AN EXTENSION OF THE ATHENA++ CODE FRAMEWORK FOR GRMHD BASED ON ADVANCED RIEMANN SOLVERS AND STAGGERED-MESH CONSTRAINED TRANSPORT. *Astrophys. J. Suppl. Ser.*, 225, 2016. doi: 10.3847/0067-0049/225/2/22. URL <http://iopscience.iop.org/ezproxy.princeton.edu/article/10.3847/0067-0049/225/2/22/pdf>.
- [78] H Spruit. Accretion Disks. In I. Martinez-Pais, T. Shahbaz, and J. Velazquez, editors, *Accretion Process. Astrophys.*, chapter 1, pages 1–44. Cambridge University Press, 2014.
- [79] N. Shakura and R. Sunyaev. Black Holes in Binary Systems. Observational Appearance. *Astron. Astrophys.*, 24:337–355, 1973.
- [80] Steven A Balbus and John F Hawley. Instability, turbulence, and enhanced transport in accretion disks. *Rev. Mod. Phys.*, 70(1):1–53, 1998. ISSN 0034-6861. doi: 10.1103/RevModPhys.70.1. URL <http://adsabs.harvard.edu/cgi-bin/nph-data?query=bibcode=1998RvMP...70...1B&link=&type=ABSTRACT&5Cnpapers://0be24a46-325a-4116-a3c6-fd8a3b614472/Paper/p9932%5Cnhttp://link.aps.org/doi/10.1103/RevModPhys.70.1>.
- [81] B Paczynski. A Model of Self-gravitating Accretion Disk. *Acta Astron.*, 28(2):91–109, 1978. URL <http://articles.adsabs.harvard.edu/cgi-bin/nph-iarticle?query=1978AcA...28...91P&defaultprint=YES&filetype=.pdf>.
- [82] James M Stone, James E Pringle, and Mitchell C Begelman. Hydrodynamical non-radiative accretion flows in two dimensions. *Mnras*, 322:461–472, 1999.
- [83] R.D. Blandford and R. L. Znajek. Electromagnetic extraction of energy from Kerr Black Holes. *Mon. Not. R. astr. Soc.*, 179:433–456, 1977.
- [84] A. Koenigl. Self-similar models of magnetized accretion disks. *Astrophys. J.*, 342:208–223, 1989.
- [85] S. Shapiro. Accretion onto Black Holes: The Emergent Radiation Spectrum. *Astrophys. J.*, 180:531–546, 1973.
- [86] John Balbus, Steven; Hawley. A Powerful Local Shear Instability in Weakly Magnetized Disks I. Linear Analysis. *Astrophys. J.*, 376:214–222, 1991.
- [87] John Hawley and Steven Balbus. A Powerful Local Shear Instability in Weakly Magnetized Disks II. Nonlinear Evolution. *Astrophys. J.*, 376:223–233, 1991.
- [88] J. Hawley and S. Balbus. A Powerful Local shear instability in weakly magnetized Disks: III. Long-Term evolution in a shearing sheet. *Astrophys. J.*, 400:595–609, 1992.
- [89] M. Kunz. AST 521 Homework 4, 2016.
- [90] M. Kunz. Notes on the Boussinesq Approximation, 2016.
- [91] Steven A. Balbus and John F. Hawley. Is the Oort A-value a universal growth rate limit for accretion disk shear instabilities? *Astrophys. J.*, 392:662–666, 1992. ISSN 0004-637X. doi: 10.1086/171467.
- [92] John F. Hawley, Charles F. Gammie, and Steven a. Balbus. Local Three-dimensional Magnetohydrodynamic Simulations of Accretion Disks. *Astrophys. J.*, 440:742, 1995. ISSN 0004-637X. doi: 10.1086/175311.
- [93] J. Hawley, C. Gammie, and S. Balbus. Local Three-Dimensional Simulations of an accretion disk hydro-magnetic dynamo. *Astrophys. J.*, 464:690–703, 1996.
- [94] S Fromang and J Papaloizou. Astrophysics MHD simulations of the magnetorotational instability in a shearing box with zero net flux I . The issue of convergence. *Astron. Astrophys.*, 1122:1113–1122, 2007.
- [95] Ji-Ming Shi, James M Stone, and Chelsea X Huang. Saturation of the magnetorotational instability in the unstratified shearing box with zero net flux: convergence in taller boxes. *MNRAS*, 456:2273–2289, 2016. doi: 10.1093/mnras/stv2815.

- [96] Timothy P Fleming, James M Stone1, and John F Hawley. THE EFFECT OF RESISTIVITY ON THE NONLINEAR STAGE OF THE MAGNETOROTATIONAL INSTABILITY IN ACCRETION DISKS. *Astrophys. J.*, 530:464–477, 2000. URL <http://iopscience.iop.org/article/10.1086/308338/pdf>.
- [97] Jacob B Simon, John F Hawley, and Kris Beckwith. SIMULATIONS OF MAGNETOROTATIONAL TURBULENCE WITH A HIGHER-ORDER GODUNOV SCHEME. *Astrophys. J.*, 690:974–997, 2009. doi: 10.1088/0004-637X/690/1/974.
- [98] Jacob B Simon and John F Hawley. VISCOUS AND RESISTIVE EFFECTS ON THE MAGNETOROTATIONAL INSTABILITY WITH A NET TOROIDAL FIELD. *Astrophys. J.*, 707:833–843, 2009. doi: 10.1088/0004-637X/707/1/833.